Thermal simulation of an experimental high temperature fixed bed cored brick regenerative air preheater
by Timothy Allen Ameel

A thesis submitted in partial fulfillment of the requirements for the degree of MASTER OF SCIENCE in Mechanical Engineering
Montana State University

Abstract:

A model was developed to simulate the thermal response of an experimental high temperature fixed bed cored brick regenerative air preheater. The experimental air preheater has been designed to study problems associated with the use of air preheaters in magnetohydro-dynamic power generation. The model simulates the experimental preheater core, in which the heat exchange between gas and ceramic take's place, by use of finite-difference equations. The insulation and steel shell surrounding the core are thermally coupled with the core by using a second set of finite-difference equations. Included in the modelling are vertical gaps between adjacent insulation layers which provide additional resistance to heat transfer and the inclusion of the gaps provides for a better representation of the entire air preheater.

Three modes of operation were simulated. During the start-up simulation, the time, burner operation, and intermediate blowdown cycles necessary to reach a steady state operating condition from room temperature were determined. During steady state simulation, the response of the insulation to change in core temperature was studied. It was determined that the first layer of insulation, the containment tube, must be considered to be part of the core thermal mass. During the cooldown simulation, the amount of time for which a back-up power source would have to operate in the event of a power failure was determined.

STATEMENT OF PERMISSION TO COPY

In presenting this thesis in partial fulfillment of the requirements for an advanced degree at Montana State University, I agree that the Library shall make it freely available for inspection. I further agree that permission for extensive copying of this thesis for scholarly purposes may be granted by my major professor, or, in his absence, by the Director of Libraries. It is understood that any copying or publication of this thesis for financial gain shall not be allowed without my written permission.

Signature Tim Arnell

Date May 31, 1977

THERMAL SIMULATION OF AN EXPERIMENTAL HIGH TEMPERATURE FIXED BED CORED BRICK REGENERATIVE AIR PREHEATER

by

TIMOTHY ALLEN AMEEL

A thesis submitted in partial fulfillment
of the requirements for the degree

of

MASTER OF SCIENCE

in

Mechanical Engineering

Approved:

H. W. Townes
Chairperson, Graduate Committee

Dennis O. Blackketter
Head, Major Department

Henry L Parsons
Graduate Dean

MONTANA STATE UNIVERSITY
Bozeman, Montana

May, 1977

ACKNOWLEDGMENTS

The author acknowledges Dr. Harry W. Townes for his assistance in preparing this thesis. The author gratefully acknowledges financial support from ERDA/MHD Division. A special thanks goes to the author's wife and parents for their guidance and support.

TABLE OF CONTENTS

Page

LIST OF TABLES

LIST OF FIGURES

NOMENCLATURE

Symbol	Description	
a	Constant defined in Table 1	
A	Average area of two surfaces forming a gap	
A_1	Area of inner surface	
A_2	Area of outer surface	
b	Constant defined in Table 1	
c	Constant defined in Table 1	
C_p	Specific heat	[J/Kg-K]
d	Constant defined in Table 1	
g	Acceleration due to gravity	
Gr_L	Grashof number based on total length	
Gr_x	Grashof number based on distance from the leading edge	
Gr_δ	Grashof number based on gap width	
h	Heat transfer coefficient	[W/m^2-K]
$\overline{h}_c$	Average heat transfer coefficient for a vertical cylinder	
h_{cx}	Local heat transfer coefficient for a vertical cylinder at a distance x from the leading edge	
i	Radial node index	
j	Time index	
k	Thermal conductivity	[W/m-K]
k_c	Thermal conductivity of insulation	
L	Length of vertical gap	

Symbol	Description	
$\overline{Nu}_L$	Average Nusselt number based on total length of a vertical cylinder	
Nu_δ	Nusselt number based on gap width	
Pr	Prandtl number	
$\dot{q}$	Heat rate	[W]
$\dot{q}_{in}$	Heat rate into an increment	[W]
$\dot{q}_{out}$	Heat rate out of an increment	[W]
$\dot{q}_s$	Heat storage rate within an increment	[W]
r_i	Radial position of node i	
Δr_i	Radial length step size for a particular layer of insulation	
r_1	Gap inside radius	
r_2	Gap outside radius	
R	Radius	
t	Time	
Δt	Time step size	
$T_{i,j}$	Insulation temperature at radial location i and time j	
T_K	Temperature (K)	
T_∞	Temperature of preheater surroundings	
T_1	Temperature of gap inside surface	
T_2	Temperature of gap outside surface	
TCB	Temperature of the core at the bottom of the preheater bed	
TCT	Temperature of the core at the top of the preheater bed	

Symbol	Description
TG	Temperature of gas in core flow holes
V	Volume
VG	Mean velocity of gas in core flow holes
x	Distance from leading edge of a vertical cylinder
Y	Thermophysical property defined in Table 1
ΔZ	Axial length step size
α'_{12}	Parameter defined in Equation (35)
α_{13}	Parameter defined in Equation (36)
α_{14}	Parameter defined in Equation (37)
α_{15}	Parameter defined in Equation (38)
α_{16}	Parameter defined in Equation (54)
α_{17}	Parameter defined in Equation (61)
α_{18}	Parameter defined in Equation (50)
α_{19}	Parameter defined in Equation (60)
β	Volume coefficient of expansion
δ	Gap width
ε_i	Emissivity of insulation material located at node i
ε_1	Emissivity of inside surface of a gap
ε_2	Emissivity of outside surface of a gap
ρ	Density
σ	Stefan-Botzmann Constant
μ	Fluid dynamic viscosity [Pa-sec]

ABSTRACT

A model was developed to simulate the thermal response of an experimental high temperature fixed bed cored brick regenerative air preheater. The experimental air preheater has been designed to study problems associated with the use of air preheaters in magnetohydrodynamic power generation. The model simulates the experimental preheater core, in which the heat exchange between gas and ceramic takes place, by use of finite-difference equations. The insulation and steel shell surrounding the core are thermally coupled with the core by using a second set of finite-difference equations. Included in the modelling are vertical gaps between adjacent insulation layers which provide additional resistance to heat transfer and the inclusion of the gaps provides for a better representation of the entire air preheater.

Three modes of operation were simulated. During the start-up simulation, the time, burner operation, and intermediate blowdown cycles necessary to reach a steady state operating condition from room temperature were determined. During steady state simulation, the response of the insulation to change in core temperature was studied. It was determined that the first layer of insulation, the containment tube, must be considered to be part of the core thermal mass. During the cooldown simulation, the amount of time for which a back-up power source would have to operate in the event of a power failure was determined.

I. INTRODUCTION

The proposed open magnetohydrodynamic (MHD) cycles of the ECAS Study [1] require a gas temperature in the MHD channel of approximately 2800 K, which is well above the gas temperature of 1900 K possible by combustion of air and a fossil fuel. There are several methods which can be used to achieve the gas temperature required in the open cycle MHD channels. One possibility is the use of oxygen enrichment, although this method is economically questionable due to the large amount and high cost of oxygen required. A second possibility is preheating of the combustion air prior to the combustion process.

Preheating of the combustion air can be accomplished using high temperature air preheaters which utilize the thermal energy of the MHD channel exhaust gas as a heat source. Several types of preheaters have been suggested for use in open MHD cycles, including pebble bed regenerators and falling bed preheaters. A third type, which has been studied here, is a fixed bed cored brick regenerative air preheater.

There are two basic problems which must be addressed when considering a fixed bed cored brick air preheater. First, the MHD channel exhaust gas contains particulates which are highly corrosive. The particulate matter includes coal slag from the combustion process and alkali metal compounds of the seed material, either cesium or potassium. Second, as the exhaust gas cools in the preheater, the alkali metal compounds and slag deposit and solidify to some extent on the walls of the flow passages. To study the deposition rate and corrosive effects of the particulate matter, an experimental fixed bed cored brick air preheater has been designed that closely models a full size air preheater.

The experimental air preheater consists of a column of hexagonal ceramic bricks containing nineteen, 19.1 mm diameter holes through which the hot gas and cool air alternately flow. Surrounding the core brick are six layers of several types of ceramic insulating materials, a steel shell, and a layer of fiberglass insulation over the steel shell. Figures 1 and 2 show the details of the experimental air preheater design.

There are several problems which must be considered when extending the results from the experimental air preheater to a full-scale preheater. One such problem is the difference in size. The ratio of external surface area to volume of the hexagonal core is inversely proportional to the radius of an inscribed circle. Therefore, for the experimental air preheater, which has a smaller core, the ratio of surface area to volume is larger than that for a full-scale preheater. Consequently, the percentage of heat transferred from the gas to the core that is transferred from the core to the surrounding insulation is larger for the experimental preheater. This larger percentage is comparable to a core with an equal number of flow passages but with more mass. The effect of heat transfer from the core to the surrounding insulation will be studied here as it is important to understand how the operation of the experimental air preheater can be related to a full-scale preheater. In particular, the relationship of the percentage of heat from the gas that is transferred to the insulation versus the axial location and time for steady state cyclic operation will be investigated.

The insulation design is also critical as it must provide sufficient resistance to heat transfer to reduce heat loss to the environment. At the same time, the insulation must allow necessary heat transfer to occur so that the temperature within the steel shell remains above the dew point temperature of the vapor near the vessel wall. This is an important requirement since the ceramic insulating materials will soften and start to break down when brought into contact with water.

The primary intent of this investigation is to determine heat losses and temperature histories throughout the experimental preheater so as to better define the interaction between the core and the surrounding insulation. A finite-difference numerical technique was developed for modelling the insulation of the experimental preheater and a separate finite-difference model was previously developed for modelling the hexagonal core. By combining the two finite-difference models, the operation of the experimental preheater can be studied. For a steady state cyclic process, results presented include the percent of heat from the gas that is transferred to the insulation versus time and axial location in the preheater. Also included are temperature histories, both axially and radially, during a steady state cycle. A start-up procedure was studied to determine the time and manner in which the experimental preheater can be brought up to the steady state condition. Also a controlled cooldown process was studied to determine the time and air temperature required to reduce the temperature of the preheater to ambient conditions without incurring damage to the ceramic bricks due to thermal shock.

II. LITERATURE REVIEW

The thermal simulation of an experimental fixed bed air preheater includes the effect of heat transfer from the relatively small core to the insulation. In a full scale preheater, this effect is negligible due to the larger core. For this reason most investigators, concerned with simulating a full sized packed bed air preheater, have only simulated the core section and have neglected radial heat transfer to the insulation.

Several investigations of regenerative air preheaters have been reported. Nusselt [2], Heiligenstaedt [3], Rummel [4], and Hausen [5] all obtained solutions to the differential equations defining the operation of a regenerative air preheater. However, the lengthy calculations involved in applying these solutions to obtain fluid and matrix temperatures make them impractical to use. A summary of the early mathematical modelling of regenerators is given by Edwards et al. [6].

More recent work in this area has been done using numerical techniques for solution of the governing differential equations. Manrique and Cardenas [7] have used a finite-difference method to calculate air bed temperatures in checkerwork regenerators. A pebble bed regenerator was modelled by El-Rifai et al. [8] again using a finite-difference method. The work by El-Rifai et al. gives very good insight; but, according to the authors, the number of simplifying assumptions decreased the accuracy of the results. Zakkay et al. [9]

have used a similar approach in modelling the core of a regenerator having a matrix of cylindrical flow holes arranged in a hexagonal pattern, much the same as that used in this investigation.

The insulation of a high temperature ceramic air preheater can represent a significant fraction of the total ceramic cost and weight. The design of the insulation in a regenerative air preheater, in which the operating temperature of the metal pressure shell was the dominant factor, has been studied by Cook [10]. The method used equated the heat transfer per unit heat exchanger length in the axial direction with the sum of the radiative and convective heat transfer to the surroundings. The relationships examined included the total insulation thickness required as a function of thermal conductivities of each layer, the diameter of the heat exchanger matrix, and the emissivity of the metal shell. Cook was primarily concerned with the optimization of the insulation design and did not study the effect of this design on the operation of the air preheater.

All of the investigators listed here have examined the response of the core or the insulation during regenerator operation. However, none have combined the two to simulate an entire regenerator. In the present investigation the heat transfer between the core and the insulation is included in the model, thereby coupling the response of the core and the insulation. With this addition, the calculation of temperature histories in the fluid, the ceramic core, and the insulation is possible simultaneously.

III. THEORY

To simulate the operation of the experimental air preheater, it is necessary to develop a model for the energy transfer in both the core and the insulation. In the core, the energy transfer from the hot fluid to the cold fluid includes intermediate energy storage in the ceramic core material. During the reheat phase of operation, the hot gas from the MHD channel passes through the preheater, transferring energy to the ceramic core. During the blowdown phase of operation, the energy stored in the ceramic core is transferred to the cooler counterflow gas stream. The operation of the core has been modelled by Reihman et al. [11] using a finite-difference method to calculate the temperature variation of the fluid and the ceramic along the axis of the heat exchanger. The model by Reihman et al. was used in this investigation to simulate the core.

In the construction of a fixed bed air preheater, the ceramic insulation is packed loosely between the central core and the steel shell to allow for the necessary thermal expansion. Even after the thermal expansion has occurred, vertical gaps still exist between adjacent radial layers of insulation. These nonuniform vertical gaps provide additional resistance to heat transfer in the insulation of the air preheater. The vertical gaps were included in the insulation geometry to obtain a more realistic representation of the insulation.

Figure 3 shows an example of the type of geometry used in the modelling of the experimental preheater.

The first attempt at modelling the insulation was an implicit method utilizing an analytical solution for the temperature profile in a circular solid ring with known heat flux boundary conditions at the inside and outside radii of the ring. From this solution the temperature of the inside and outside boundary of an insulation layer were known in terms of the heat fluxes in and out of the layer. Combining this with the heat fluxes which are known in terms of the temperature of the insulation boundaries, a set of non-linear simultaneous equations results which can then be solved for the temperatures and heat fluxes at a particular axial location in the preheater. This method was discontinued when it proved to be too time consuming and expensive for use on a digital computer.

A finite-difference numerical technique was next selected to model the insulation. For ease of computer coding, the same number of nodes were used in each radial layer of insulation in the finite-difference formulation. A simplifying assumption was made that the thermal resistance of the steel shell was considered negligible. For this reason there are no nodes in the steel shell layer for the finite-difference formulation. Figure 3 indicates the type of node structure used.

As noted previously, heat transfer across the vertical gaps is included in this model. This heat transfer occurs by the combination of natural convection, conduction, and radiation. The natural convection heat transfer coefficient for a vertical cylindrical space was approximated by an empirical equation for natural convection in the air space between two isothermal walls as presented by Jakob [12]. This approximation of a cylindrical air space by an air space between two flat plates is suggested by Jakob as the best approximation when

$$L/\delta \gg 1 \tag{1}$$

where

L = length of the vertical gap (m)
δ = width of the gap (m)

The Nusselt number Nu_δ for natural convection in a vertical gap was taken as

$$Nu_\delta = h\delta/k \tag{2}$$

where

h = heat transfer coefficient ($W/m^2 - K$)
k = thermal conductivity of the gas in the gap ($W/m - K$)

The Nusselt number is based on the Grashof number Gr_δ for heat transfer in vertical spacings. The Grashof number is given by

$$Gr_\delta = \rho^2 g\beta(T_1-T_2)\delta^3/\mu^2 \tag{3}$$

where

ρ = gas density (Kg/m^3)
g = acceleration due to gravity, 9.8 m/sec^2
β = volume coefficient of expansion (K^{-1})$\sim$1/T for an ideal gas
T_1 = temperature of wall 1 (K)
T_2 = temperature of wall 2 (K)
μ = dynamic viscosity (Pa - sec)

The equations giving the free convection heat transfer coefficients are given by Jakob as

$$\overline{Nu}_\delta = \begin{cases} 0.18Gr_\delta^{1/4}(L/\delta)^{-1/9} & \text{for } 2x10^3<Gr_\delta<2x10^4 \quad (4) \\ 0.065Gr_\delta^{1/3}(L/\delta)^{-1/9} & \text{for } 2x10^4<Gr_\delta<11x10^6 \quad (5) \end{cases}$$

where $\overline{Nu}_\delta$ denotes an average Nusselt number. For a Grashof number less than 2000, the process is simple conduction and the following equation applies

$$\overline{Nu}_\delta = h\delta/k = 1.0 \tag{6}$$

Equations (4), (5), and (6) include the effects of conduction and natural convection. Therefore, the heat transferred across a vertical gap by conduction and natural convection is given by

$$\dot{q} = h\ (T_1 - T_2)\ A \tag{7}$$

where

$\dot{q}$ = heat rate (W)
A = average area of the two surfaces (m^2)

Holman [13] gives an equation for radiation heat transfer between two concentric cylinders of infinite length in which the shape-factor is one, as

$$\dot{q} = \sigma A_1(T_1^4 - T_2^4)/[1/\varepsilon_1 + (A_1/A_2)(1/\varepsilon_2 - 1)] \tag{8}$$

where

σ = Stefan-Boltzmann Constant = 5.669×10^{-8} W/m^2-K^4
A_1 = inside surface area (m^2)
A_2 = outside surface area (m^2)
ε_1 = inside surface emissivity
ε_2 = outside surface emissivity

For the case where the concentric cylinders have a finite length and the gaps are small in comparison with the diameter of the inside cylinder, the effect of the axial temperature profile on the total radiation received by one finite element can be neglected, and Equation (8) can be used as an approximation.

Conduction is the only mode of heat transfer that occurs in a solid. For a cylindrical solid ring with a temperature T_1 at the inside radius and a temperature T_2 at the outside radius, Holman [13] gives the following equation for the resulting heat transfer rate:

$$\dot{q} = 2\pi k_c L(T_1 - T_2)/\ln(r_2/r_1) \tag{9}$$

where

k_c = thermal conductivity of the solid (W/m-K)
L = axial length of element (m)

At the outer wall of the preheater, heat is lost by a combination of radiation and natural convection. Siegel and Howell [14] give an equation for the radiative heat transfer of a gray isothermal body with an area A_1 and temperature T_1 completely enclosed by a much larger gray isothermal enclosure having area A_2 as

$$\dot{q} = A_1 \varepsilon_1 \sigma (T_1^{\,4} - T_2^{\,4}) \tag{10}$$

In the case of a preheater placed in a large room, T_2 would equal the room temperature.

Kreith [15] gives the following equation for the local value of the heat transfer coefficient for laminar free convection from an isothermal vertical cylinder at a distance x from the leading edge:

$$h_{cx} = 0.41k/x(Pr \cdot Gr_x)^{1/4} \qquad \text{for } 10<Gr_L Pr<10^9 \tag{11}$$

where Pr is the Prandtl number. The leading edge is the lower edge for a heated surface. In the turbulent region, the value of h_{cx}, the local heat transfer coefficient, is nearly constant over the surface. Therefore, McAdams [16] recommends for $Gr \geq 10^9$ the equation

$$\overline{Nu}_L = \overline{h}_c L/k = 0.13(Gr_L Pr)^{1/3} \tag{12}$$

Kreith also states that for laminar free convection from a vertical cylinder, the equations apply for a constant surface temperature as well as to a uniform heat flux over the surface.

With the simplifying assumption that axial heat conduction is negligible in the insulation, the finite-difference equations can be developed by application of the First Law of Thermodynamics which may be expressed as:

$$\begin{Bmatrix}\text{rate of increase of}\\ \text{internal energy of system}\end{Bmatrix} = \begin{Bmatrix}\text{rate of heat}\\ \text{transfer into system}\end{Bmatrix} - \begin{Bmatrix}\text{rate of work done by surface}\\ \text{forces (pressure and shear forces)}\\ \text{on the surroundings}\end{Bmatrix} \tag{13}$$

Equation (13) is called the energy equation and in developing the finite-difference equations, the work term is negligible. For more details of the development of the finite-difference equations, see Appendix I.

For a node at the inside of a radial insulation layer, the heat entering the element is the heat that is transferred through the gap adjacent to the element. Again, it was assumed that the axial conduction in the fluid was negligible. Heat leaves the element by conduction radially through the solid. By application of the energy equation, the resulting finite-difference equation is given by

$$T_{i,j+1} = T_{i,j} + 1/\alpha_{15}(i)\{\alpha_{13}(i)[T_{i-1,j}-T_{i,j}] + \alpha_{12}(i)[T_{i-1,j}{}^4 - T_{i,j}{}^4] - \alpha_{14}(i)[T_{i,j}-T_{i+1,j}]\} \quad (14)$$

where

i = radial node index
j = time index
T = temperature (K)

$$\alpha_{12}(i) = \sigma(3r_{i-1}-r_{i-2})/2[1/\varepsilon_{i-1}+(3r_{i-1}-r_{i-2})/(3r_i-r_{i+1})\mathrm{x}(1/\varepsilon_i-1)]$$

$$\alpha_{13}(i) = h(3r_{i-1}-r_{i-2}+3r_i-r_{i+1})/4$$

$$\alpha_{14}(i) = k_c(i)/\ell n[(r_i+r_{i+1})/(3r_i-r_{i+1})]$$

$$\alpha_{15}(i) = \rho(i)C_p(i)r_i(r_{i+1}-r_i)/\Delta t$$

r_i = radial position of node i (m)
$k_c(i)$ = thermal conductivity of insulation (W/m-K)
$\rho(i)$ = insulation density (Kg/m^3)
$C_p(i)$ = insulation specific heat (J/Kg-K)
Δt = time increment (sec)

Using the energy equation again, the equation defining the temperature of an interior node at time t+Δt in terms of surrounding node temperatures at time t can be written. The resulting equation for an interior node is given by

$$T_{i,j+1} = T_{i,j} + 1/\alpha_{15}(i)\{\alpha_{14}(i-1)[T_{i-1,j}-T_{i,j}]$$

$$- \alpha_{14}(i)[T_{i,j}-T_{i+1,j}]\} \quad (15)$$

The finite-difference equation for a node at the outside of an insulation layer can be determined by utilizing an energy balance once more. The resulting equation is

$$T_{i,j+1} = T_{i,j} + 1/\alpha_{18}(i)\{\alpha_{14}(i-1)[T_{i-1,j}-T_{i,j}]$$

$$- \alpha_{13}(i+1)[T_{i,j}-T_{i+1,j}] - \alpha_{12}(i+1)[T_{i,j}^4-T_{i+1,j}^4]\} \quad (16)$$

where

$$\alpha_{18}(i) = \rho(i)C_p(i)r_i(r_i-r_{i-1})/\Delta t$$

One more finite-difference equation is needed at the last node of the radial grid. Here the heat loss from the nodal element is by natural convection and radiation to the surroundings. By applying an energy balance, the equation for the last node is

$$T_{i,j+1} = T_{i,j} + 1/\alpha_{18}(i)\{\alpha_{14}(i-1)[T_{i-1,j}-T_{i,j}]$$

$$- \alpha_{19}(i)[T_{i,j}^4-T_\infty^4] - \alpha_{17}(i)[T_{i,j}-T_\infty]\} \quad (17)$$

where

T_∞ = temperature of surroundings (K)

$\alpha_{19}(i) = \sigma\varepsilon_i(3r_i-r_{i-1})/2$

$\alpha_{17}(i) = h(3r_i-r_{i-1})/2$

Due to the explicit technique adopted for solution of the problem, the stability of all of the finite-difference equations must be assured. For a specific minimum radial increment Δr a maximum allowable time increment Δt can be calculated. For example, with a radial grid consisting of five nodes in each insulation layer the minimum radial increment for the experimental heat exchanger geometry is 5.08 mm. The corresponding maximum allowable time increment to assure stability is 4.8 seconds. Details of the determination of stability are shown in Appendix II.

As can be seen in Equations (14) through (17), various physical properties of the insulating materials need to be known for different temperatures and positions in the model of the air preheater. These properties include thermal conductivity, specific heat, density, and emissivity. It is also evident from Equations (11) and (14) that the thermophysical properties of dynamic viscosity, thermal conductivity, and Prandtl number are needed as functions of temperature for air. All of these properties, with the exception of insulation density and emissivity which were considered invariant with temperature, were approximated from the best available data by a least squares curve fit. In most cases the form of the equation which was fitted to the available data was selected because the resulting equation gave the least amount of error over the temperature range considered.

Eight separate physical properties fitted a polynomial equation best. Air thermal conductivity and Prandtl number were best fitted using a cubic polynomial, while the thermal conductivity of the insulating bricks and fiberglass insulation were best fitted using a first degree polynomial. These equations are listed in Table 1 together with their maximum percent error, average percent error, the source of data, and the temperature range for which they are applicable.

Eight other physical properties were fitted using a power equation of the form

$$Y = aT_k^{\,b} \tag{18}$$

where

Y = physical property
T_k = temperature (K)
a,b = constants

These equations are listed in Table 2 together with a least squares error analysis that gives maximum and average percent errors for the available data, the data source, and the temperature range for which the equations were developed. It should be noted that the equation defining the specific heat of JM-3000 and JM-32 insulating materials is an approximation, as the data for specific heat was unavailable. The equation used was obtained by averaging the equations defining specific heat as a function of temperature for JM-20, JM-23, and JM-26 insulating materials.

The specific heat of the fiberglass insulation is considered to be a constant equal to 880 J/Kg-K, as the actual value remains virtually unchanged for the temperature range in which it was used. An equation is also needed for air dynamic viscosity for temperatures less than 1100 K. The power equation for this property, listed in Table 2, only applies in the temperature range of 1100 K to 1950 K. The Handbook of Heat Transfer [17] gives an equation for air dynamic viscosity in the temperature range less than 1100 K as

$$\mu = 4.0201 \times 10^{-7} + 7.458 \times 10^{-8} T_k - 5.7177 \times 10^{-12} T_k^{2} + 2.993 \times 10^{-14} T_k^{3} - 6.252 \times 10^{-18} T_k^{4} \quad (19)$$

where

μ = dynamic viscosity (Pa-sec)
T_k = temperature (K)
Max. error = 2.57%
Avg. error = 0.22%

Example plots of the various types of curve fit equations are shown in Figures 4 and 5.

IV. RESULTS

Using the analytical model developed for the experimental air preheater, several preheater modes of operation were studied. These modes included a start-up operation, steady state operation, and a rapid cooldown. The start-up simulation was run to determine the time, and reheat and intermediate blowdown schedules necessary to reach the steady state operating level beginning with the preheater at room temperature. Steady state is defined as the point in time at which the net heat loss from the preheater to the surroundings is within five percent of the net heat entering the insulation on consecutive reheat and blowdown cycles. The rapid cooldown simulation was run to determine the time for which an alternative power source would have to operate during a power failure to insure the safety of the facility.

The insulation materials and the dimensions of the facility that were used in the simulations are shown in Figure 2. The gaps between the brick insulation layers were set at 3.17 mm. No attempt was made to determine the effects of different gap sizes. In the finite-difference model, five nodes were located in each insulation layer. This number was selected after a stability analysis was performed to determine a workable number of nodes based on a trade-off between accuracy and computer run time.

The hexagonal core was approximated by a cylinder with equal exterior area. The core contained nineteen flow holes, 1.90 cm in diameter and 6.1 meters in length. The nineteen holes were simulated in the finite-difference model by using one hole and extending the result to nineteen holes. The temperature of the core outer wall was approximated by the average temperature of the ceramic surrounding the simulation flow hole.

One of the purposes of the experimental air preheater is to study the corrosive effects and deposition rates of liquid coal slag and seed particulates that a full scale preheater will be subject to in MHD power generation. To study these effects, coal slag and seed compounds will be injected into the reheat gas stream during steady state operation. Therefore, for the steady state simulations, the reheat gas properties were based on the combustion products of coal and air with an addition of an alkali metal compound seed in a quantity one percent by weight. The gas used on steady state blowdown cycles, the start-up operation, and on the cooldown operation was air.

Start-up

The purpose of the start-up is to raise the temperature of the preheater to a steady state temperature level as rapidly as possible while maintaining limits on some parameters. The maximum gas flow rate is limited to 100 SCFM on both reheat and blowdown. The maximum gas temperature available on reheat is limited to 2033 K while the maximum and minimum gas temperatures possible on blowdown are 394 K and 294 K, respectively. The design limitation on the maximum allowable ceramic temperature at the bottom of the core is 811 K. The maximum allowable thermal stress for the core material was unknown at the time of the simulations. However, in laboratory tests performed at Montana State University, it was determined that the maximum allowable indicated thermal stress was on the order of 7.0×10^7 pascals. This high stress level is due to the fact that the ceramic core material is initially non-homogeneous and contains many small cracks which help to relieve thermal stresses and, consequently, the actual stress does not approach the theoretically calculated value. However, once the core has been exposed to the alkali metal compounds and slag contained in the reheat gas, these cracks will become impregnated with the liquid particulates and the allowable stress level will be reduced.

The main objective of the start-up simulation is to obtain a temperature profile in the core that closely resembles the core temperature profile after a reheat cycle during steady state operation. The radial temperature profiles in the insulation are of secondary importance. After completion of the start-up simulation, at which point the core temperature profile resembles that for steady state, cycling of the preheater using steady state parameters will allow the insulation to be raised to steady state levels.

From steady state simulations a temperature profile in the core was obtained which was to be matched during the start-up operation. For the steady state operation the temperature at the top of the core, TCT, was 1815 K and the temperature at the bottom of the core, TCB, was 761 K. It was decided during the start-up simulation to allow TCB to reach the maximum allowable temperature of 811 K since during cycling needed to raise the temperature level of the insulation to a steady state level, TCB will drop with each successive reheat cycle due to heat loss from the core to the insulation.

The first step in the start-up simulation was a bake cycle in which 394 K blowdown air at maximum velocity was used to raise the temperature of the entire bed while removing any moisture that is present. This cycle is completed when TCT equals 377 K. Next, 2033 K reheat air at maximum velocity is used to raise TCT as rapidly as possible and also to obtain the largest temperature difference between TCT and TCB. This cycle is completed when TCB reaches the maximum allowable temperature of 811 K. Now a series of alternating blowdown and reheat cycles are begun during which TCB is first reduced 167 K and then raised to 811 K. With each successive reheat cycle TCT increases, until after thirty-eight cycles TCT reaches the required temperature of 1815 K. Table 3 lists the flow parameters, cycle times, and temperature limits for all of the start-up cycles.

Figure 6 shows the core temperature profile at several times during the start-up simulation. Figure 7 shows the radial temperature profile 2.1 cm from the top of the core during the start-up simulation. It should be noted that there is a large difference in the radial temperature profiles between the end of start-up and steady state. Even after 16 hours of operation, the outer layers of insulation have just begun to experience an increase in temperature. No attempt was made to determine the time required to reach steady state, due to the amount of computer run time necessary.

Steady State

The purpose of the experimental air preheater is to study the operating conditions, some of which have been outlined in the ECAS Study, for full scale preheaters to be used in MHD application. ECAS Open Cycle MHD Base Case 1 has typical operating conditions and was selected for simulation using the finite difference numerical model.

Since the exit gas temperature, TG, on reheat in Base Case 1 is specified as 1478 K, only part of the overall length of the experimental preheater is needed to model this particular case. The main flow parameters, cycle times, and core temperature bounds are listed in Table 3. The flow parameters used in the simulation are not exactly those specified in Base Case 1, because the flow parameters had to be changed to force TCB to fall below the 811 K limit imposed upon it. The simulation was started using linear temperature profiles both axially and radially.

Steady state was defined as the point in time at which the net heat flux to the surroundings from the preheater was within five percent of the net heat flux from the core to the insulation during two successive reheat and blowdown cycles. Figure 8 shows how steady state was approached during the simulation run. From Figure 8 it appears that the net heat flux to the surroundings will eventually be within five percent of the net heat flux to the insulation. However, after 90 hours of simulation, it was decided, since changes were occurring so slowly and computer costs were mounting, that this point of the simulation would serve to represent steady state. After 90 hours of simulation, the difference between the net heat flux to the insulation and the net heat flux to the surroundings ranged from 17.5% at the top of the bed to -5.4% at the bottom of the bed.

Figure 9 shows the axial temperature profile in the preheater core after a steady state reheat cycle and after a steady state blowdown cycle. The upswing in the curve at the top of the bed represents an increase in temperature due to entrance effects which increase heat transfer from the gas to the core. The same holds true for the bottom of the bed but the effect is less pronounced. The large difference between TCB after reheat and after blowdown is caused by the large gas and core temperature difference at the bottom of the bed which results in more heat transfer during a particular cycle. Thus, TCB increases and decreases a greater amount than other axial locations during reheat and blowdown cycles.

Figure 10 shows the radial temperature profiles at three different axial locations after a steady state reheat cycle. The only noticeable change from these profiles and those after a blowdown cycle occurs in the core and containment tube. The rest of the insulation remains virtually unchanged during steady state operation. Figure 10 also indicates that the temperature of the steel shell is above the dew point temperature of the vapor that will be present near the steel shell. The dew point temperature was found to be approximately 303 K by a calculation similar to that performed in <u>Steam/Its Generation and Use</u> [21]. The presence of the fiberglass insulation over the steel shell helped to keep the steel shell temperature above the vapor dew point temperature.

Since each layer of insulation is homogeneous, the curves in each layer are smooth. Each point represents a node of the finite-difference model and discontinuities in the curves represent the relatively small temperature drops across the vertical gaps. The slope of the curves in each particular layer give an indication of the relative amount of heat transfer occurring at a particular axial position in the layer of insulation.

The temperature change in the insulation takes place mainly in the containment tube. Figures 11 and 12 show the temperature variation of the core and containment tube at the top of the bed during steady state blowdown and reheat cycles. The temperature profile of the containment tube closely follows the core temperature at this axial location. However, further down the bed the response of the containment tube to changes in core temperature is much less. Figure 13 shows the response of the containment tube to changes in core temperature during a steady state reheat cycle at the bottom of the bed. The difference in response of the containment tube shown in Figures 12 and 13 is due to radiation heat transfer which is more dependent on the absolute temperatures rather than the temperature difference across the gap at a particular axial location. Further evidence of the difference in response of the containment tube is shown in Figure 10. It is also evident from Figures 11, 12, and 13 that there is very little change in temperature for the outer node of the containment tube during a cycle. At the next largest radial node the temperature change is negligible.

A further indication of the coupling of the core and containment tube is shown in Figure 14. This figure gives the percentage of heat that is transferred from the core to the containment tube compared to the heat transfer from the gas to the core as a function of time during a steady state reheat cycle. The profile calculated at 27.5 seconds shows that the top half of the bed has responded to the reheat cycle while the bottom half has changed very little from the end of the previous cycle, which is shown in Figure 15. It should be noted from Figure 14 that the further down the bed the slower the response of the containment tube to the core. For the profile calculated at 27.5 seconds, only at the very top of the bed has the direction of heat transfer between the core and containment tube reversed. It takes approximately the full reheat cycle for the direction of heat transfer at the bottom of the bed to be reversed. The small percentage of heat transfer at the bottom of the bed during the cycle is another indication of the small amount of radiation heat transfer taking place.

The same arguments can be made for a similar plot of the percentage of heat transfer for a blowdown cycle as shown in Figure 15. However, here the top of the bed displays a somewhat slower response to the new cycle. This is caused by the change in gas flow direction for the blowdown cycle. The percentage of heat transfer between the gas and containment tube ranges from 50 to 5 percent at the end of a reheat cycle and from 25 to 4 percent at the end of the blowdown cycle.

Cooldown

If a power failure occurred during operation of the experimental air preheater, the gas flow in the core, which is induced by a five horsepower electric blower, would stop. When there is no gas flow, the preheater is said to be soaking. During a soak cycle, heat transfer by axial conduction takes place, raising the temperature of the ceramic at the bottom of the bed. Since the maximum allowable temperature at the bottom of the bed is 811 K, allowing the preheater to soak could result in failure of the support structure. For this reason it was necessary to determine the time required for which an alternate power source would be needed to run the five horsepower blower.

A temperature of 811 K was selected as the maximum allowable temperature in the preheater before soaking could take place. The flow rate was limited by the 100 SCFM air blower. It was assumed that the cracks in the ceramic material will have been impregnated with liquid seed and slag, thus reducing the maximum allowable thermal stress level. With these limitations, the cooldown was initiated after a steady state blowdown cycle using the maximum possible blowdown gas temperature to reduce thermal stresses. The temperature of the blowdown air was then reduced to room temperature when TCB was low enough so that the stresses produced remained low. The actual maximum resultant stress on both of the cooldown cycles was approximately 7.8×10^6 pascals. This blowdown cycle was continued until the temperature of the entire preheater was less than 811 K. Table 3 contains the flow parameters, cycle times, and temperature limits for the cooldown operation.

The highest temperature in the preheater after a steady state blowdown cycle occurs at the top of the bed. This is also the axial position that cools most slowly. Figure 16 shows the radial temperature profile at the top of the bed during the cooldown operation. The containment tube closely follows the temperature of the core. Figure 17 shows the core axial temperature profile during the cooldown operation. Using this cooldown operation in the event of a power failure, the maximum time that a back-up power source would be needed to drive the five horsepower blower would be 27.6 hours.

V. CONCLUSIONS

Based on the simulations performed using the finite-difference model, several conclusions can be made.

(1) The containment tube must be considered to be part of the core thermal mass.

(2) During a power failure, a back-up power source will be needed for approximately 28 hours to ensure safety of the facility.

(3) It will not be possible for the experimental air preheater to reach steady state in a reasonable amount of time (approximately five days).

VI. RECOMMENDATIONS

(1) A better approximation is needed for the core outer wall temperature. Including simulation of all of the flow holes would give an improved approximation for the core temperature.

(2) A better understanding of the thermal stress limits for the core material is needed.

(3) A larger core with a smaller exterior surface area to volume ratio should be used in future designs to reduce the thermal interaction between the core and the insulation.

(4) A back-up power source should be provided for the air preheater facility to power the five horsepower blower in the event of a power failure.

Table 1. Material property curve fit equations - Polynomial fit

$$Y = a + b T_k + c T_k^2 + d T_k^3$$

	Y	a $\times 10^{-1}$	b $\times 10^{-5}$	c $\times 10^{-9}$	d $\times 10^{-12}$	max. % error	ave. % error	range (K)	source of data
Air	k	0.0757	6.135	1.655	-5.406	0.96	0.29	273-1920	[15]
Air	Pr	8.008	-39.32	437.0	-126.9	2.00	1.10	311-1920	[15]
Cont. tube	k	72.31	-667.6	3130.	0.0	7.50	4.20	478-1920	[19]
JM-20 & -23	k	0.76	9.35	0.0	0.0	0.00	0.00	533-1367	[20]
JM-26	k	2.23	12.0	0.0	0.0	0.22	0.00	533-1367	[20]
JM-3000	k	3.47	8.97	0.0	0.0	2.00	0.17	533-1367	[20]
JM-32	k	4.19	5.23	0.0	0.0	3.42	0.10	533-1367	[20]
Fib. insltn.	k	2.33	23.44	0.0	0.0	1.10	0.64	283-340	[20]

k = thermal conductivity (W/m-K)
Pr = Prandtl number

Table 2. Material property curve fit equations - Power fit

$$Y = a\,T_k^{\,b}$$

	Y	a	b	max. % error	avg. % error	range (K)	source of data
Air	μ	7.445×10^{-7}	0.5818	0.28	0.15	1100-1950	[18]
Cerafelt	k	2.307×10^{-6}	1.616	5.5	2.4	590-1367	[20]
Cerafelt	C_p	173.7	0.266	0.21	0.14	367-1255	[20]
Cont. tube	C_p	281.3	0.186	0.23	0.11	533-2090	[19]
JM-20	C_p	219.7	0.231	1.7	0.76	366-1367	[20]
JM-23	C_p	175.0	0.276	3.5	1.1	366-1478	[20]
JM-26	C_p	175.8	0.270	2.1	0.86	366-1478	[20]
JM-3000 & -32	C_p	190.1	0.259	--	--	-- --	--

C_p = specific heat (J/Kg-K)
k = thermal conductivity (W/m-K)
μ = dynamic viscosity (Pa-sec)

Table 3. Simulations data

Start-up

Cycle	Inlet TG (K)	Inlet VG (m/sec)	Time (hr)	TCT (K)	TCB (K)
Blowdown 1	394	12.71	11.56	377	393
Reheat 2	2033	66.5	1.50	1769	811
Blowdown 3-37	294	9.48	0.034*	--	644
Reheat 4-38	2033	66.5	0.079*	--	811

Steady state

Cycle	Inlet TG (K)	Inlet VG (m/sec)	Time (min)	TCT (K)	TCB (K)
Blowdown	394	9.56	3.69	1762	587
Reheat	1978	50.3	4.28	1815	761

Cooldown

Cycle	Inlet TG (K)	Inlet VG (m/sec)	Time (hr)	Max. ins. temp.	TCB (K)
Blowdown 1	394	11.46	0.13	1753	464
Reheat 2	294	8.72	27.5	810	295

*Average

Explanation of Figures

Vertical dashed lines included in Figures 7, 10, and 16 illustrate the position of the insulation layers and vertical gaps. The left hand side of Figures 7, 10, and 16 corresponds to the core while the last vertical dashed line on the right hand side represents the outer surface of the fiberglass insulation. Figures 1 and 2 can be used to identify the insulation materials used at a particular axial location.

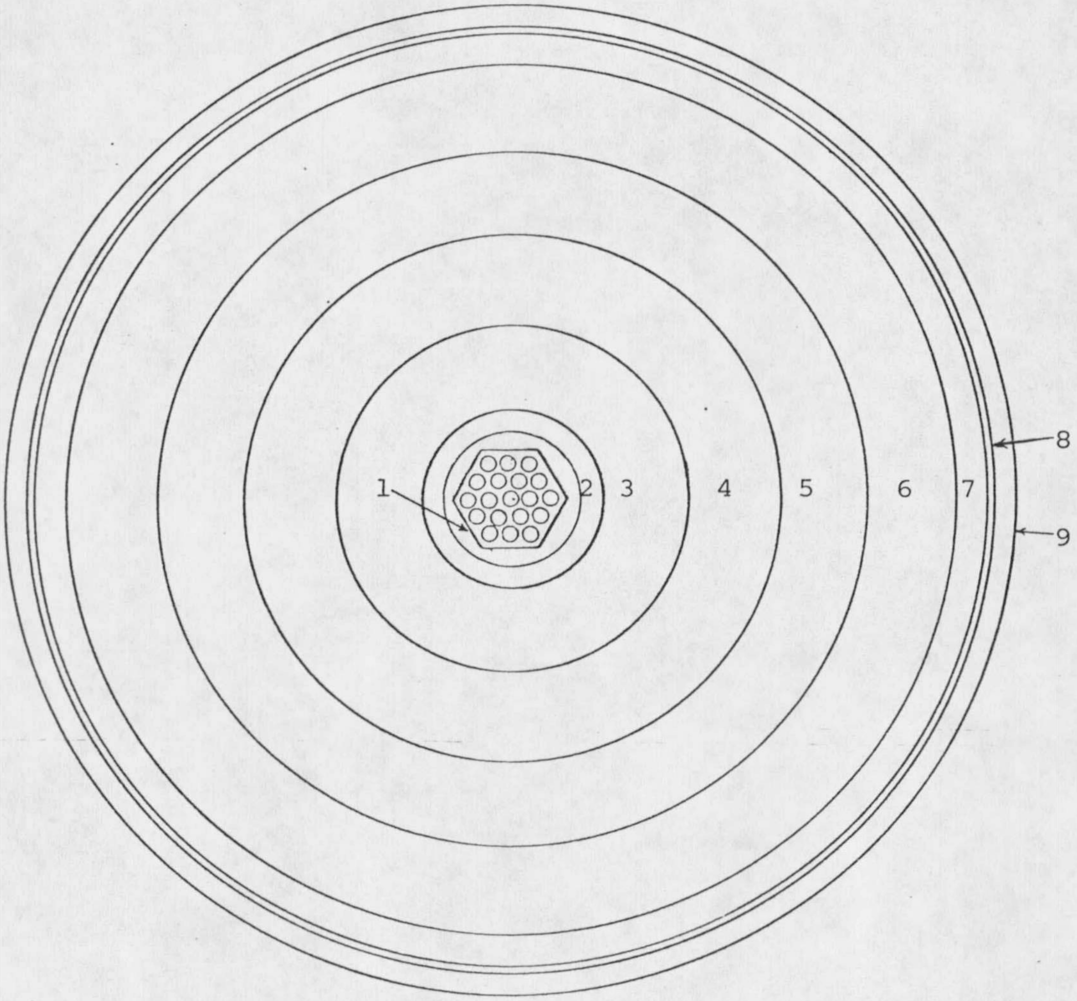

1. 19 hole core	4. JM-26	7. Cerafelt blanket
2. containment tube	5. JM-23	8. steel shell
3. JM-32	6. JM-23	9. fiberglass insulation

Figure 1. Cross section of Experimental Air Preheater One Meter from Bed Top.

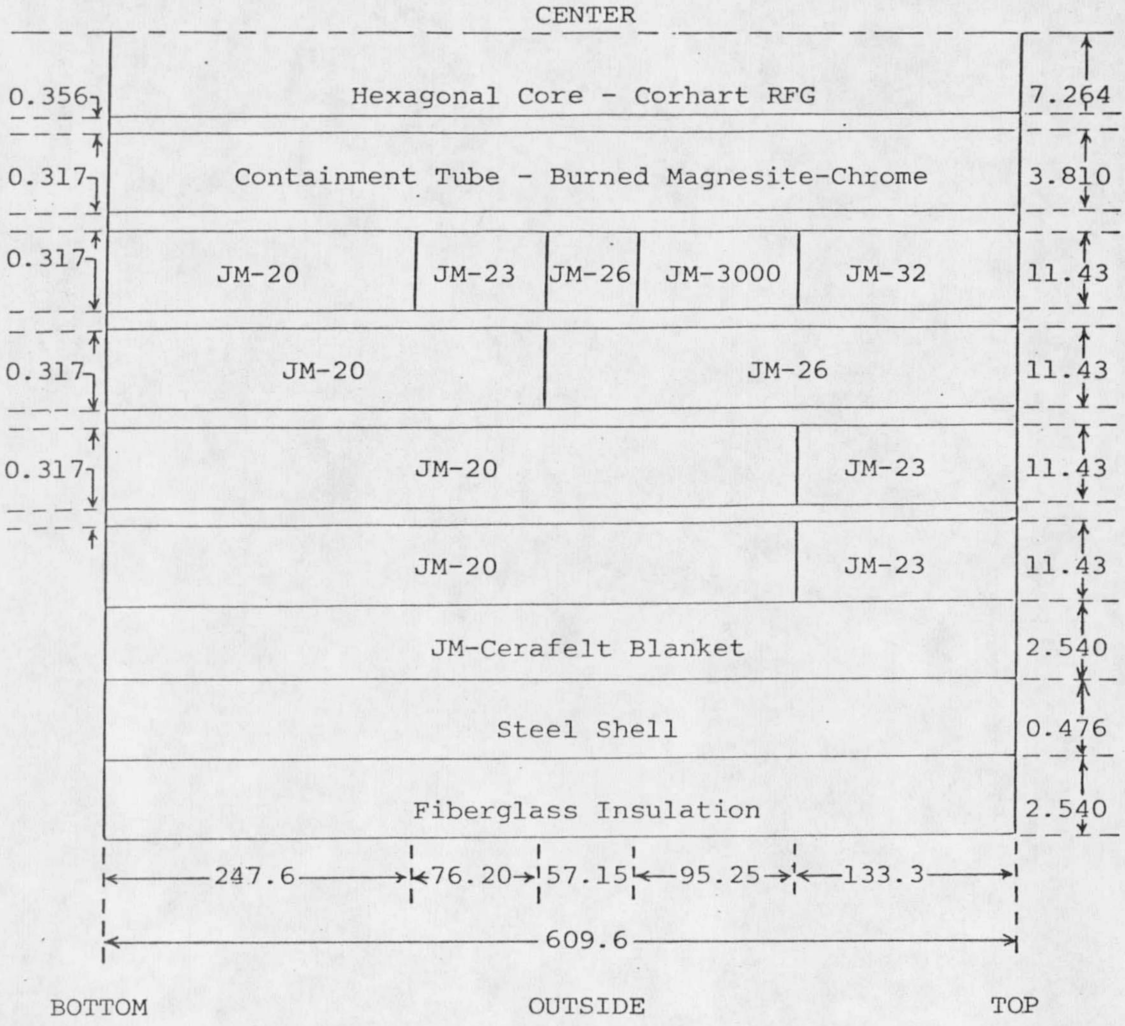

Figure 2. Experimental Air Preheater Materials and Dimensions Including Gaps.
Note: Not to scale, all dimensions in centimeters.

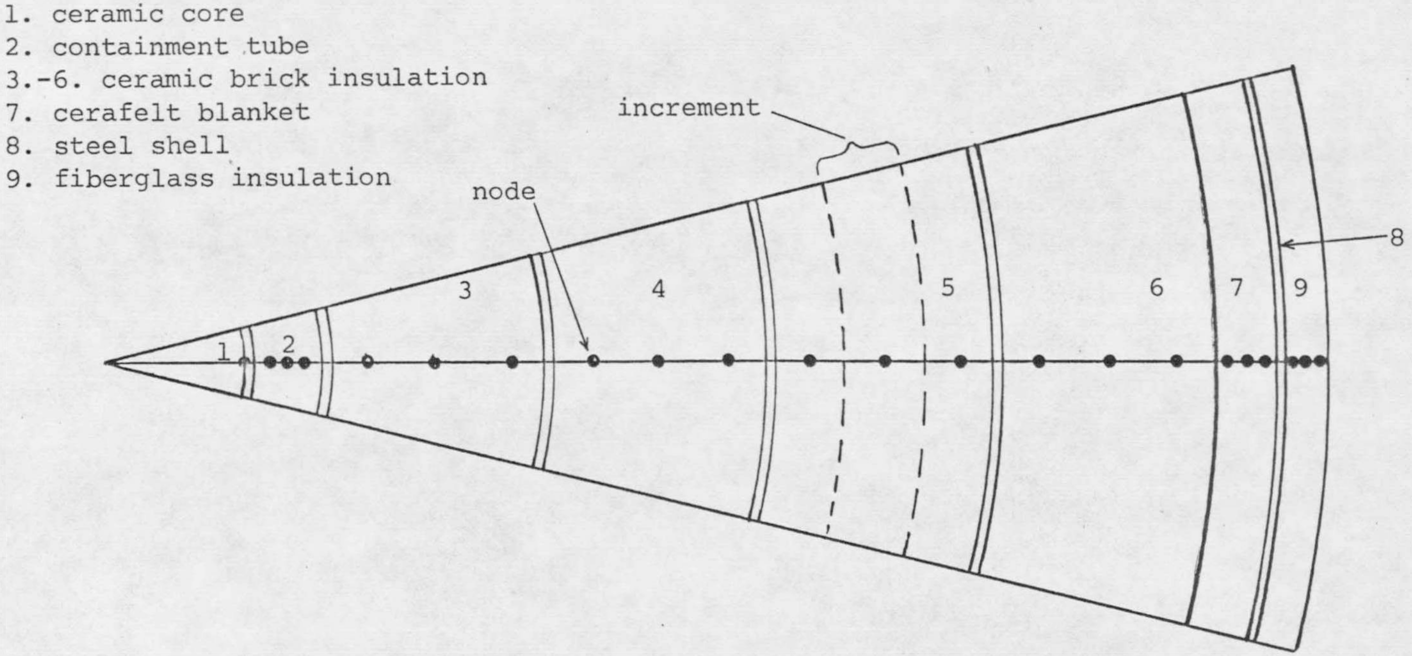

Figure 3. Example of Node Structure (3 Nodes Per Layer) for the Finite-Difference Numerical Model.

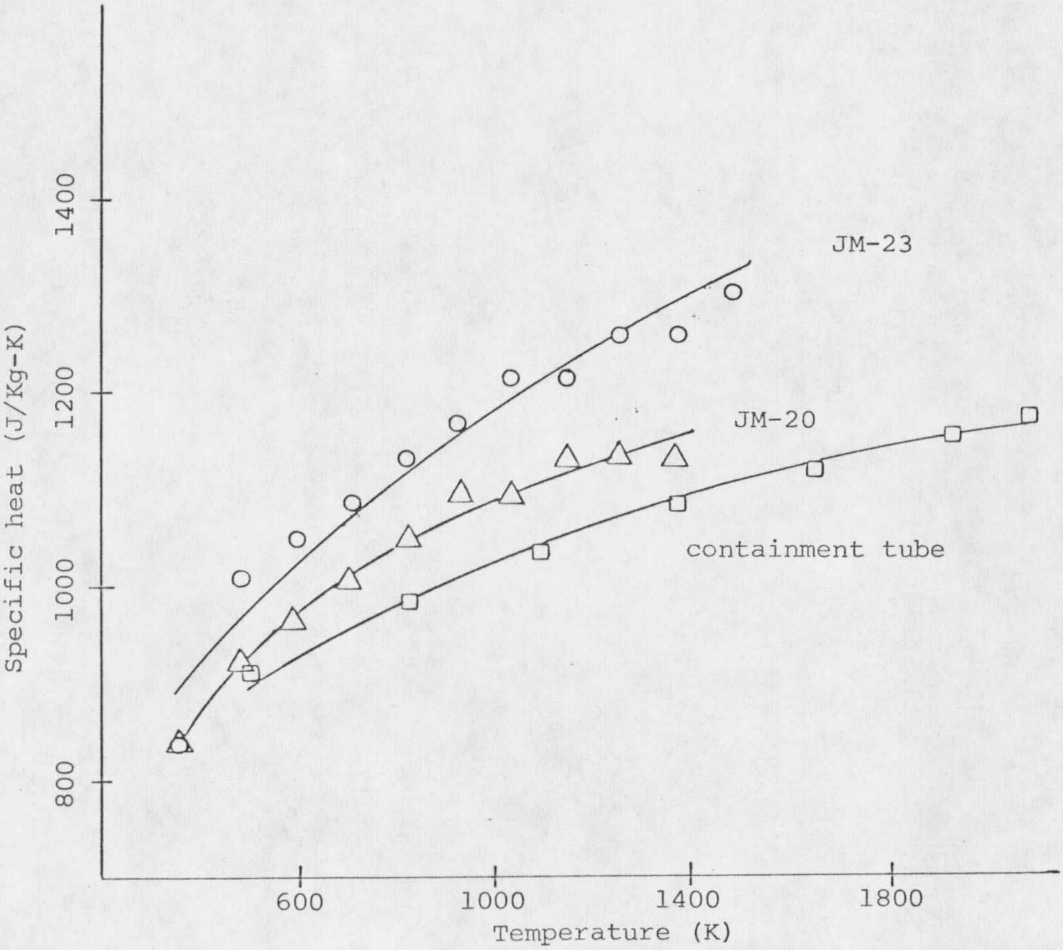

Figure 4. Examples of Specific Heat Curve Fit Equations.

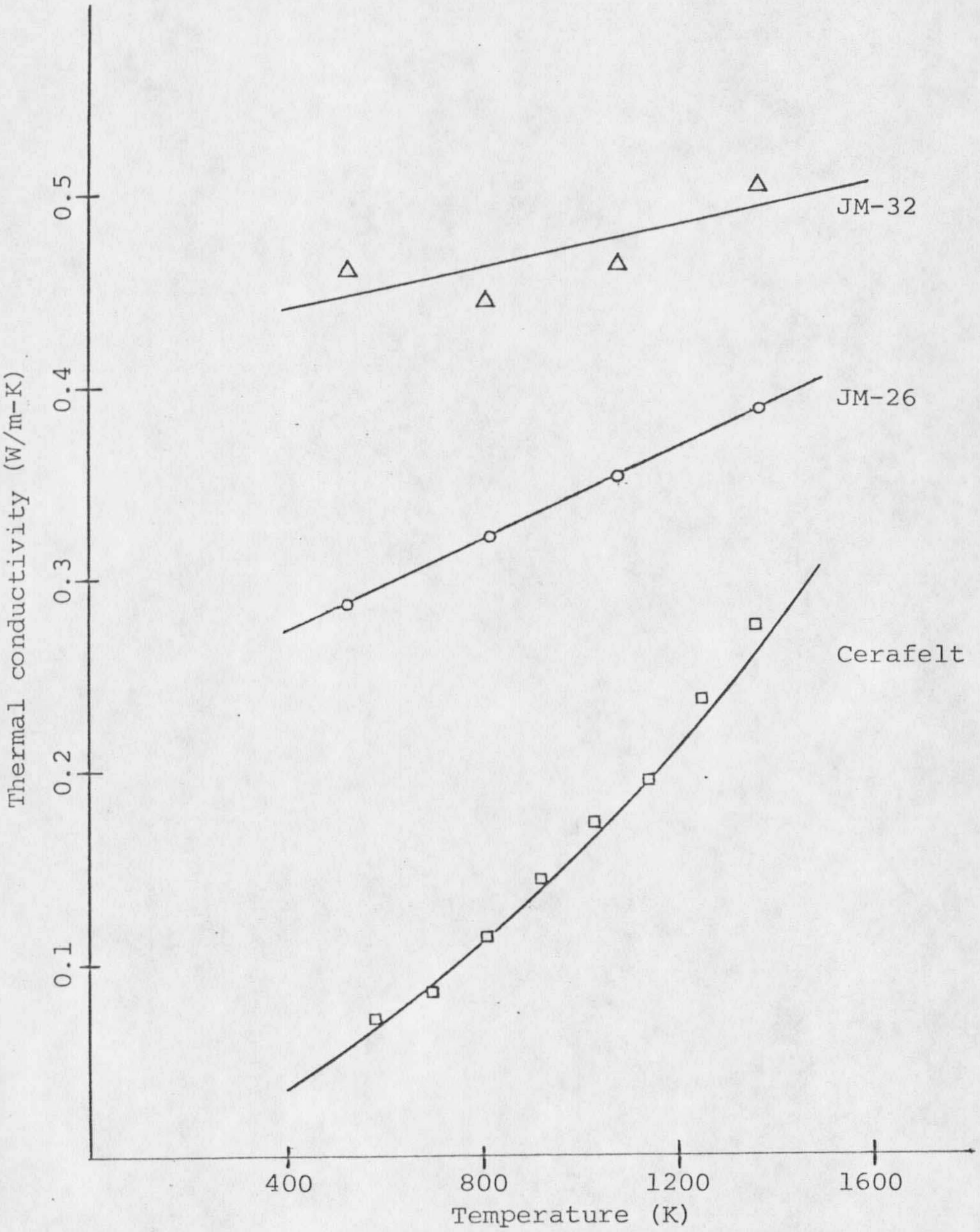

Figure 5. Examples of Thermal Conductivity Curve Fit Equations.

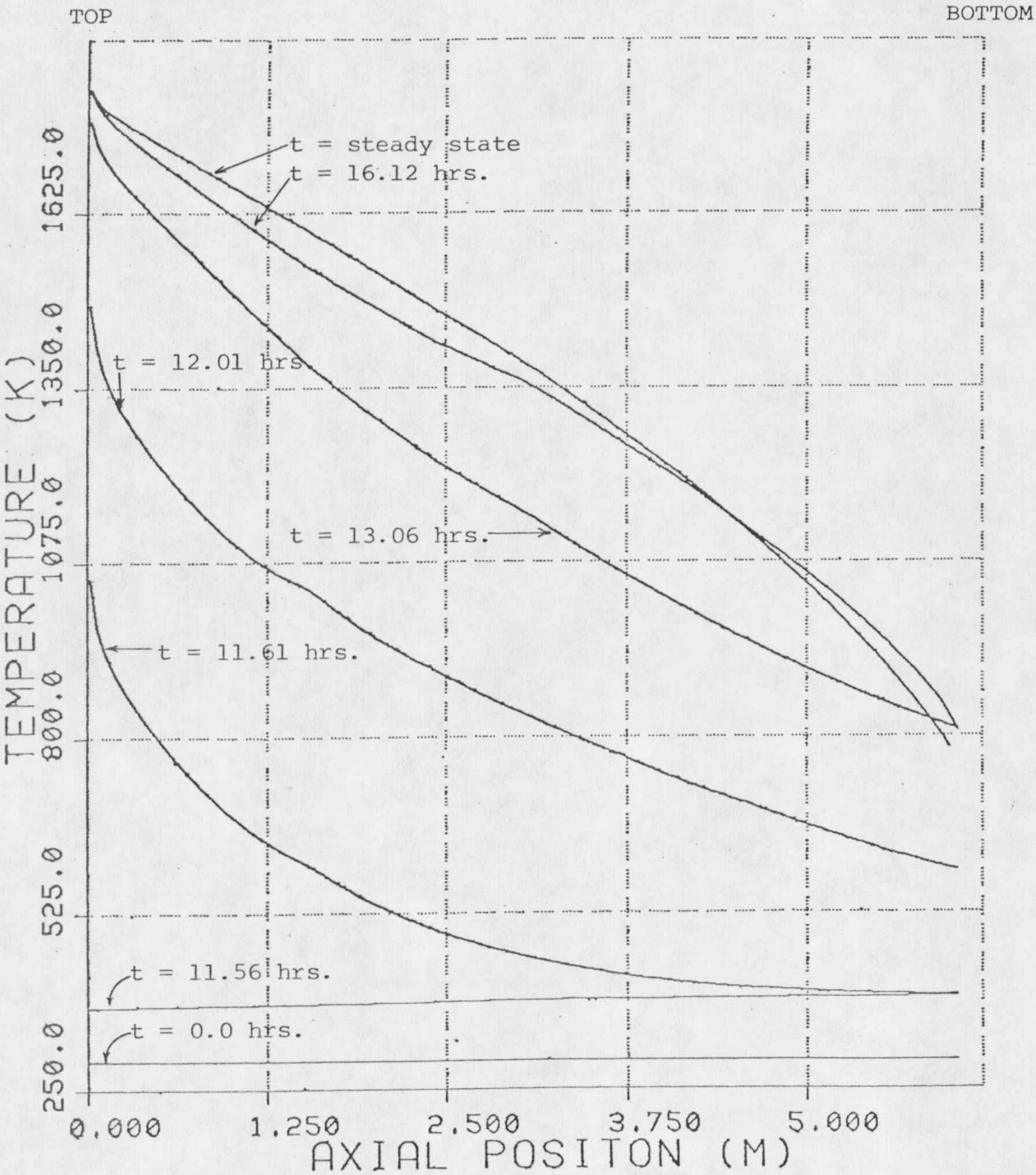

Figure 6. Axial Temperature Profile in the Preheater Core During Start-up.

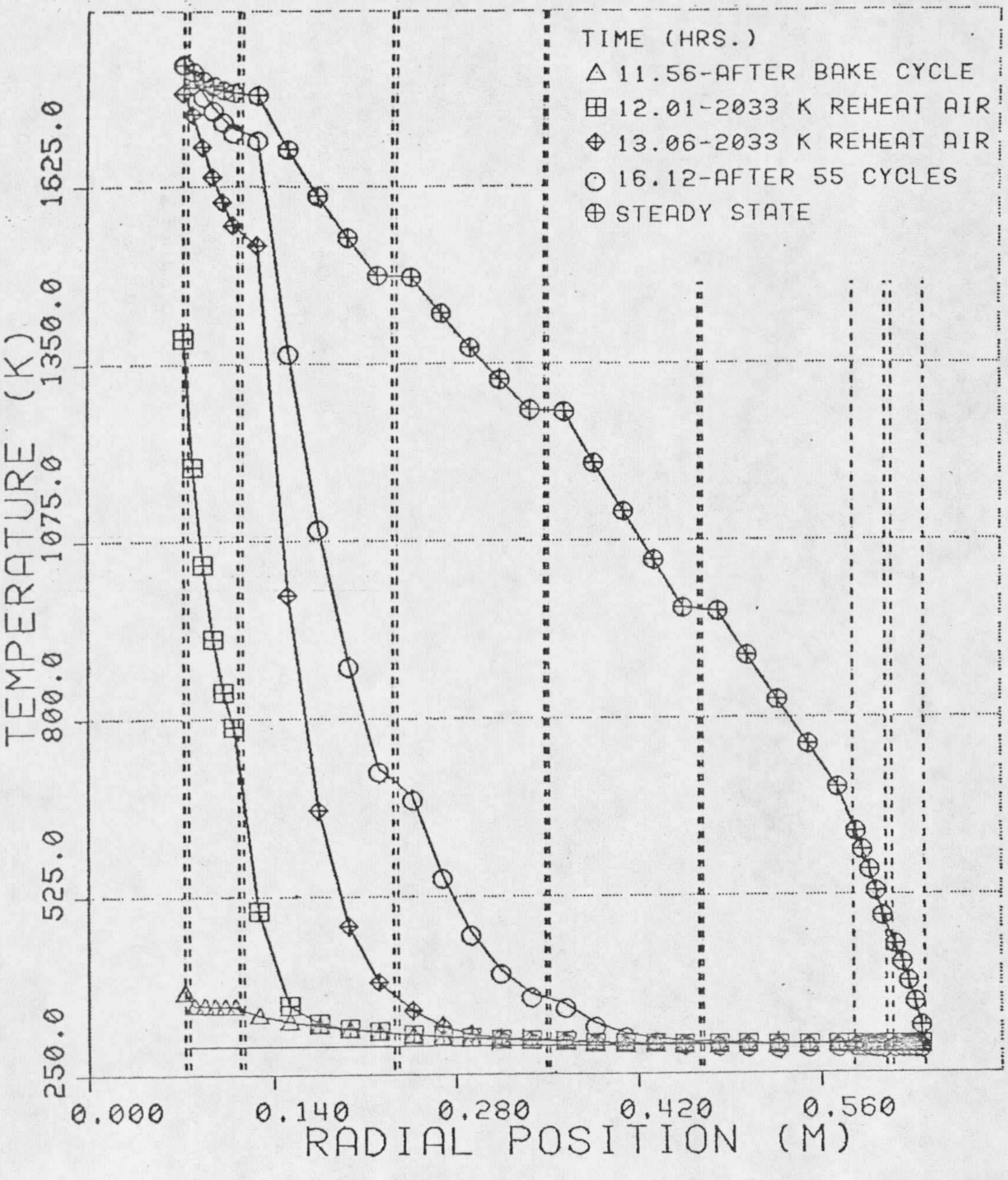

Figure 7. Radial Temperature Profile During Start-up Axial Position 2.1 cm from Bed Top.

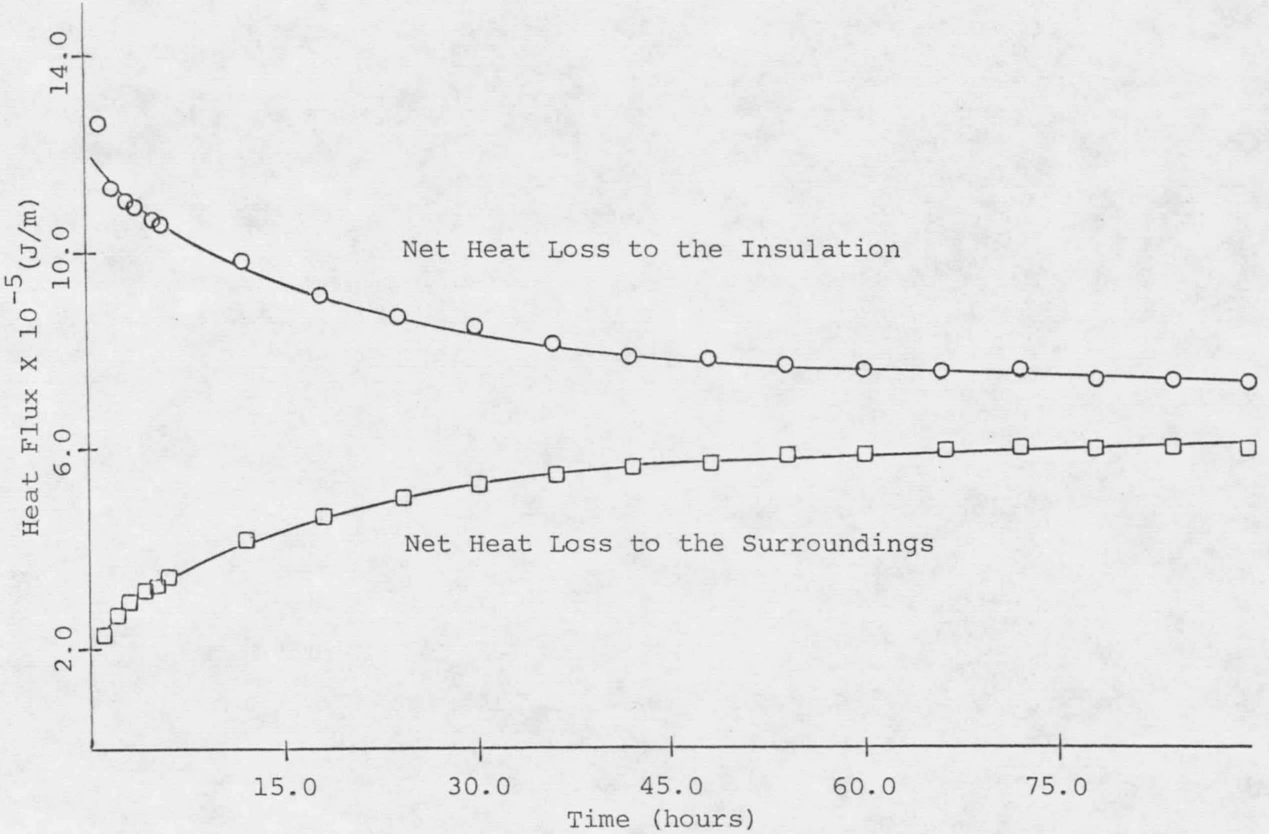

Figure 8. Heat Flux Approach to Steady State.

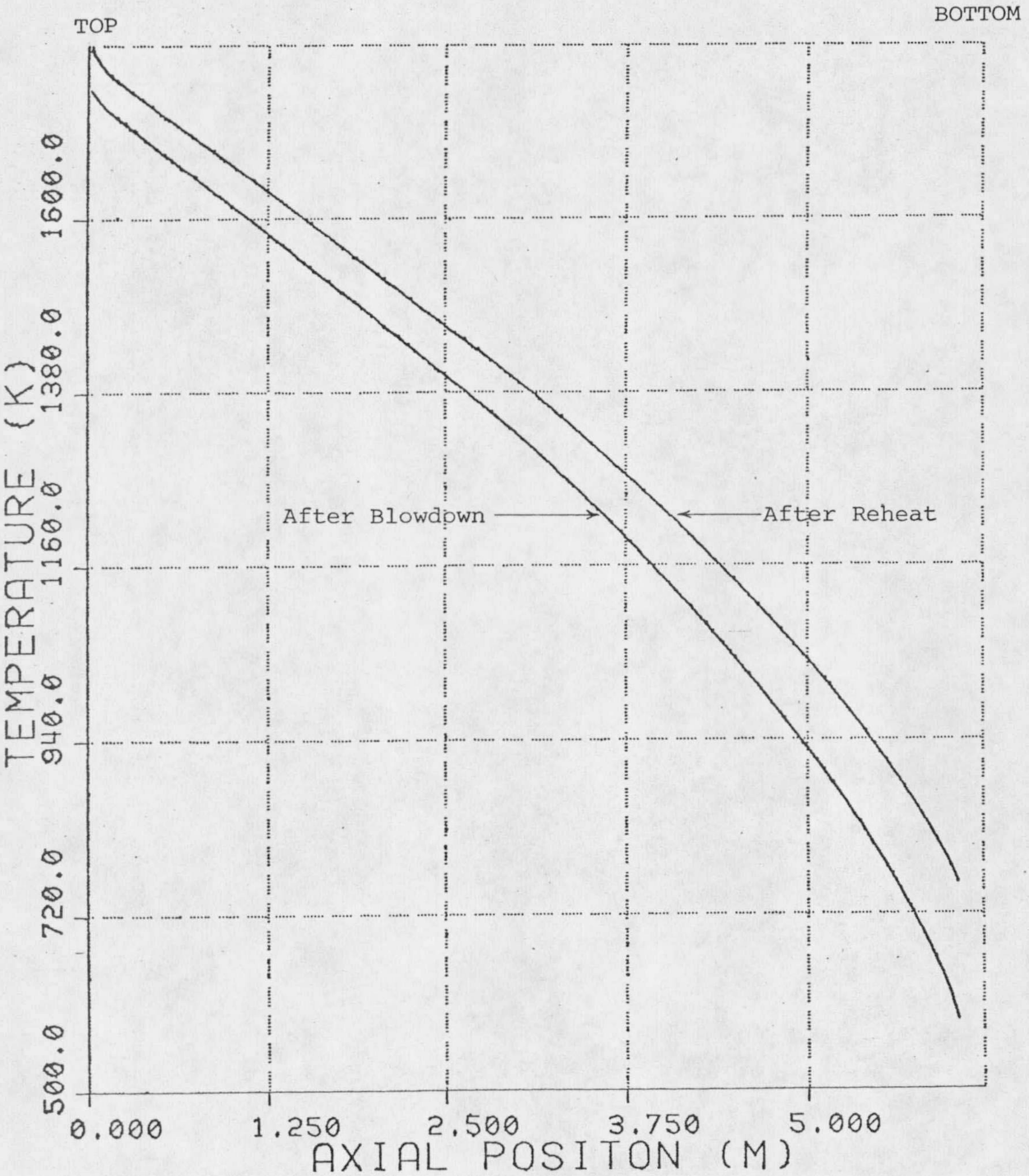

Figure 9. Axial Temperature Profile in the Preheater Core During Steady State Operation.

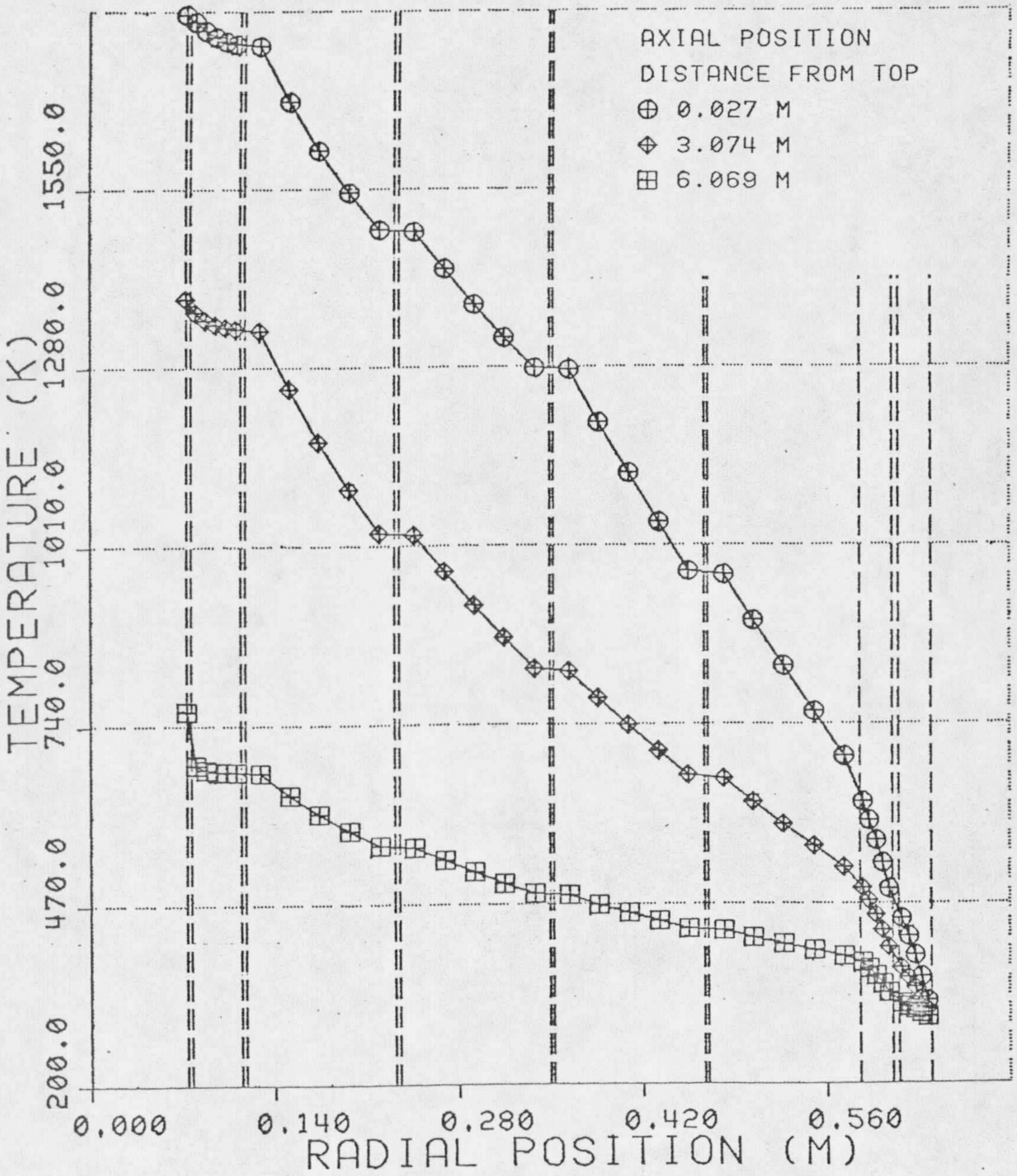

Figure 10. Radial Temperature Profiles After a Steady State Reheat Cycle at Three Axial Locations.

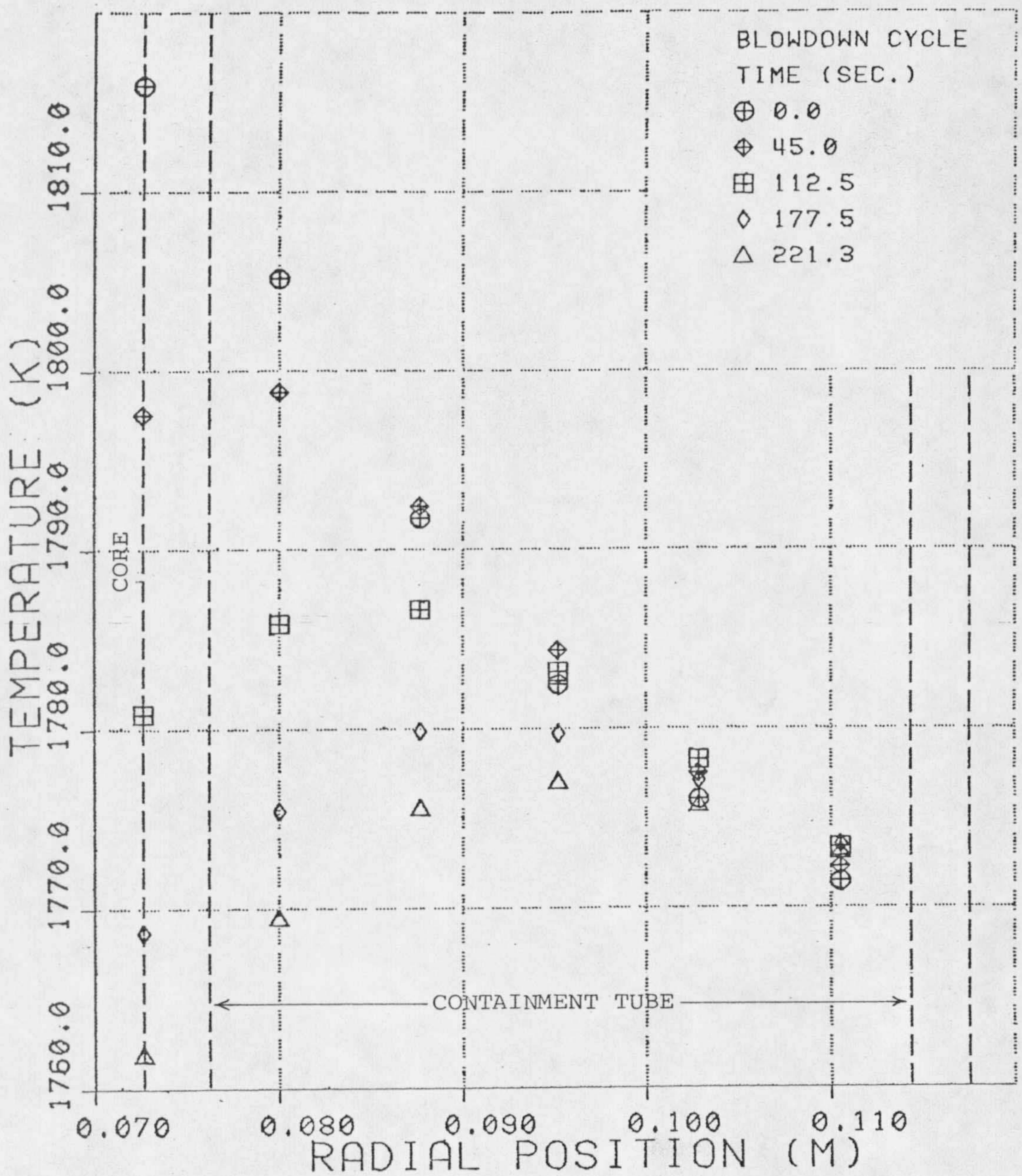

Figure 11. Temperature of the Core and Containment Tube During a Steady State Blowdown Cycle Axial Position 2.7 cm from Bed Top.

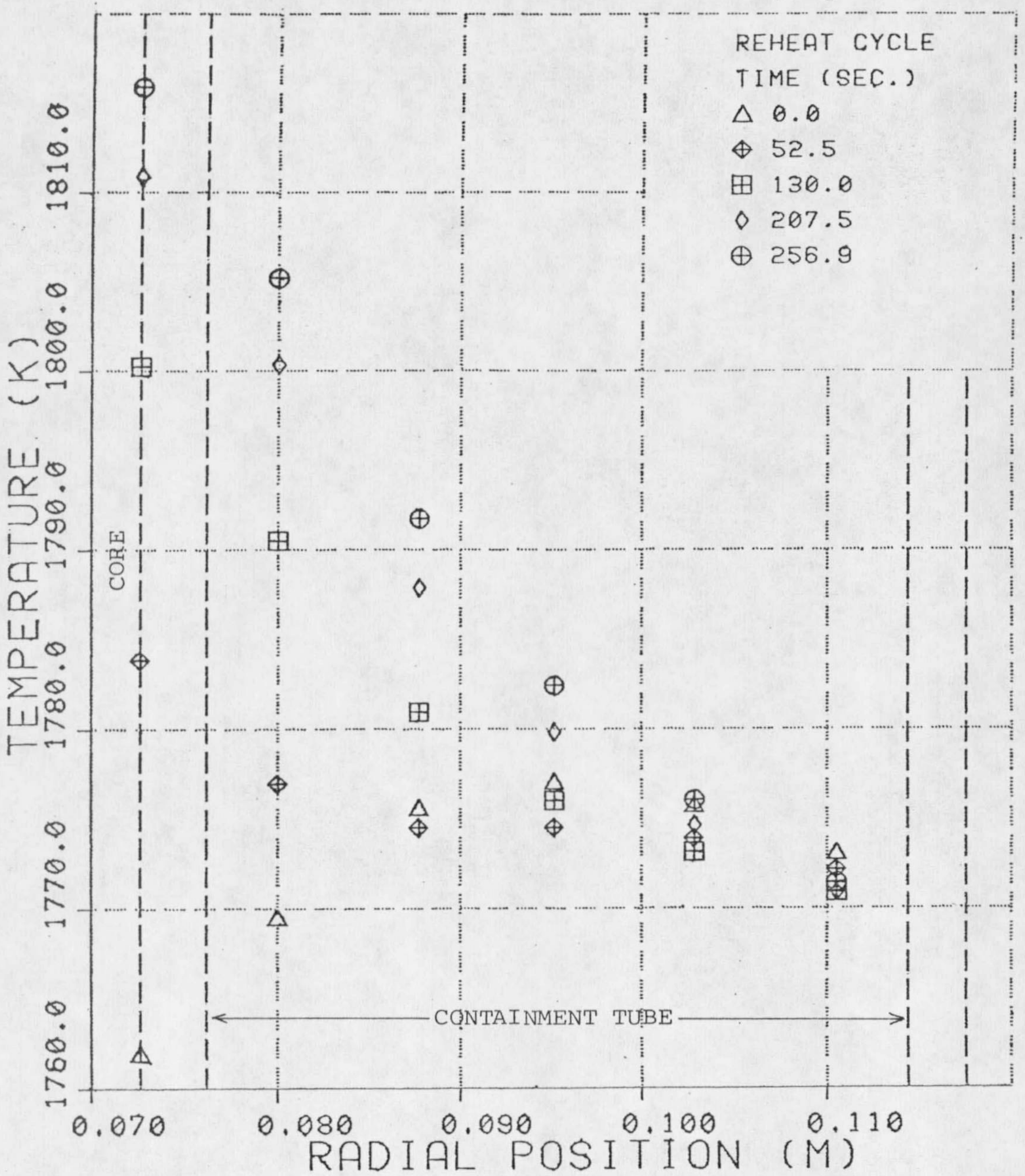

Figure 12. Temperature of the Core and Containment Tube During a Steady State Reheat Cycle Axial Position 2.7 cm from Bed Top.

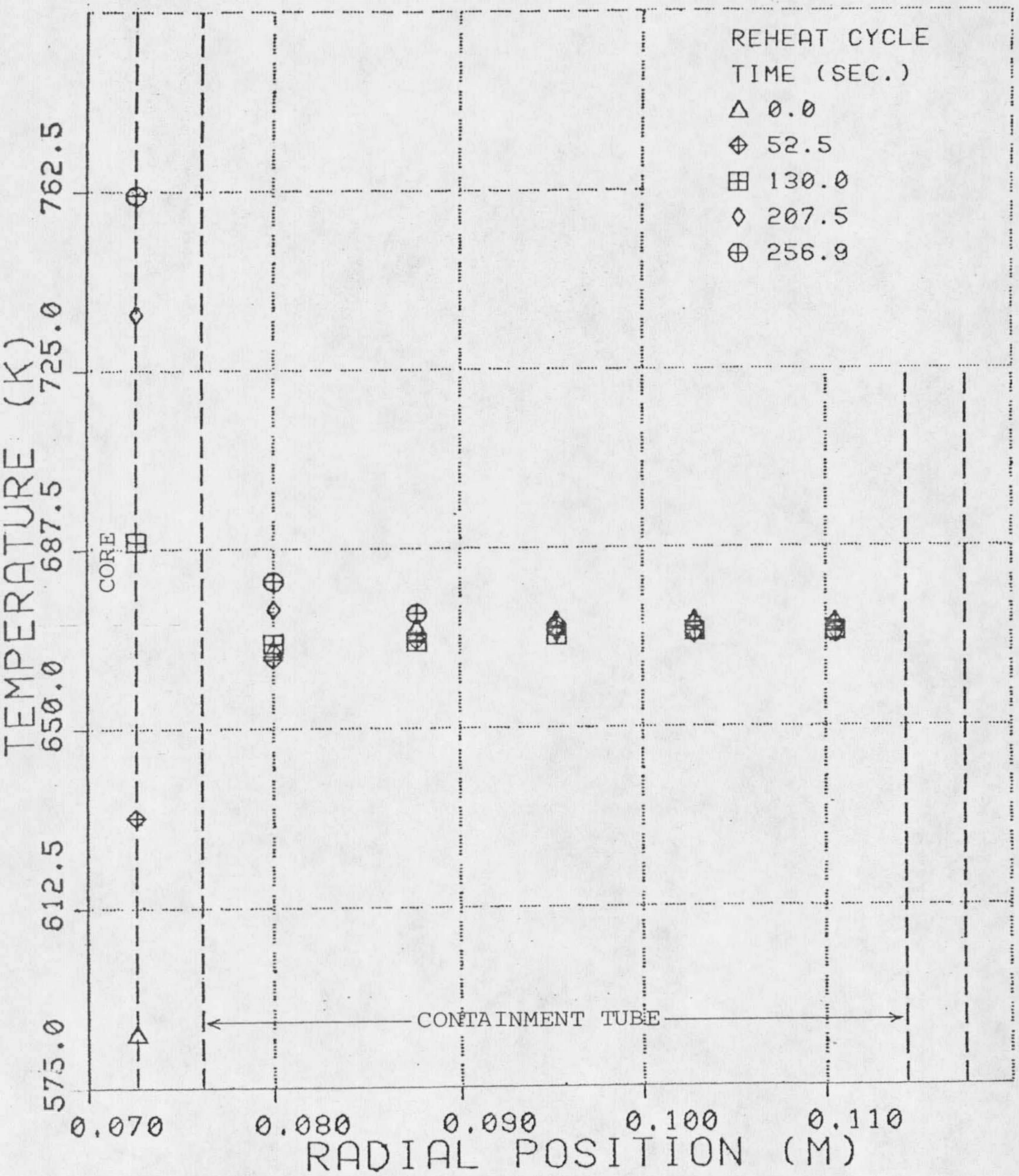

Figure 13. Temperature of the Core and Containment Tube During a Steady State Reheat Cycle Axial Position 2.7 cm from Bed Bottom.

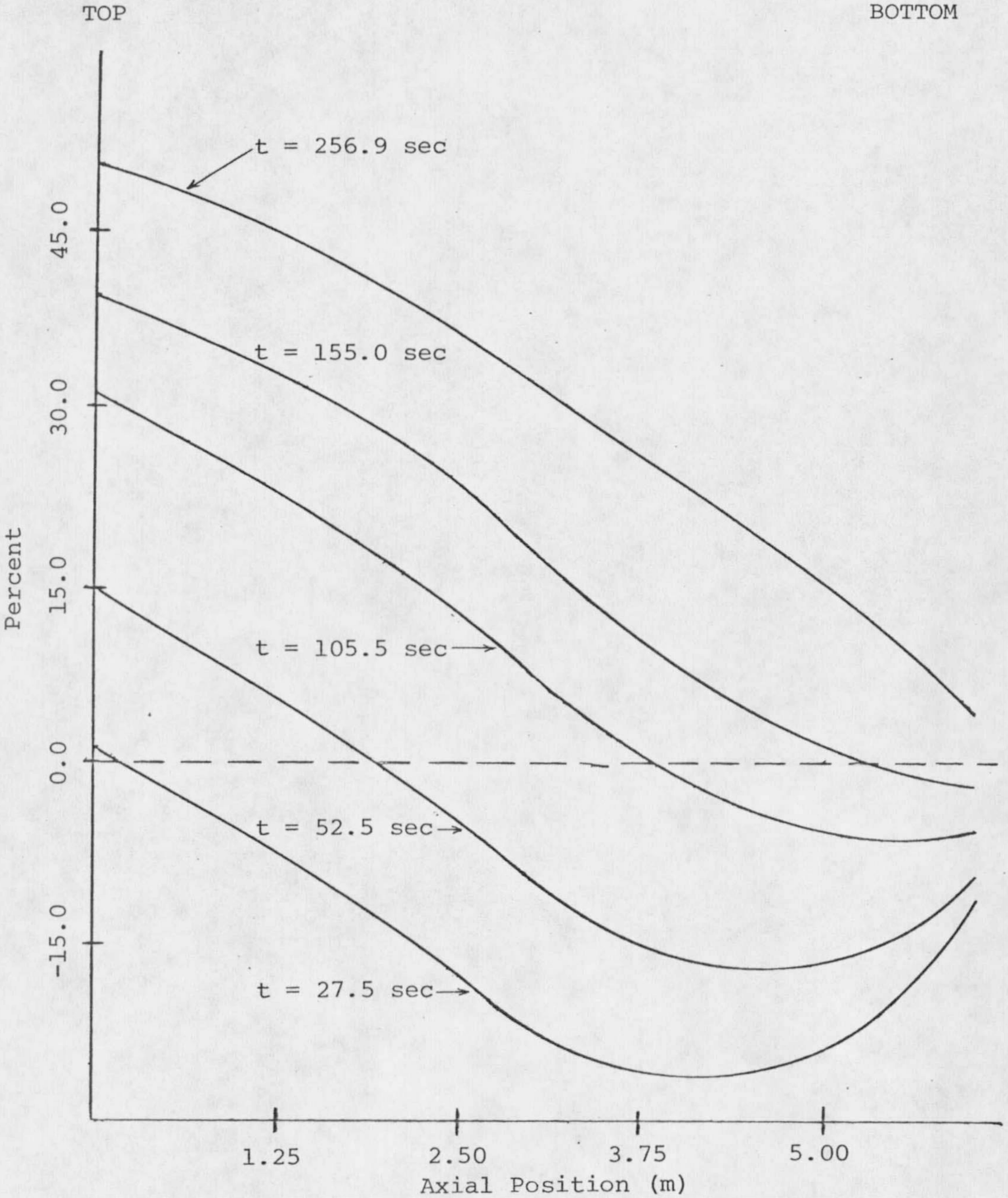

Figure 14. Percentage of Gas to Core Heat Transferred from Core to Containment Tube During a Steady State Reheat Cycle.

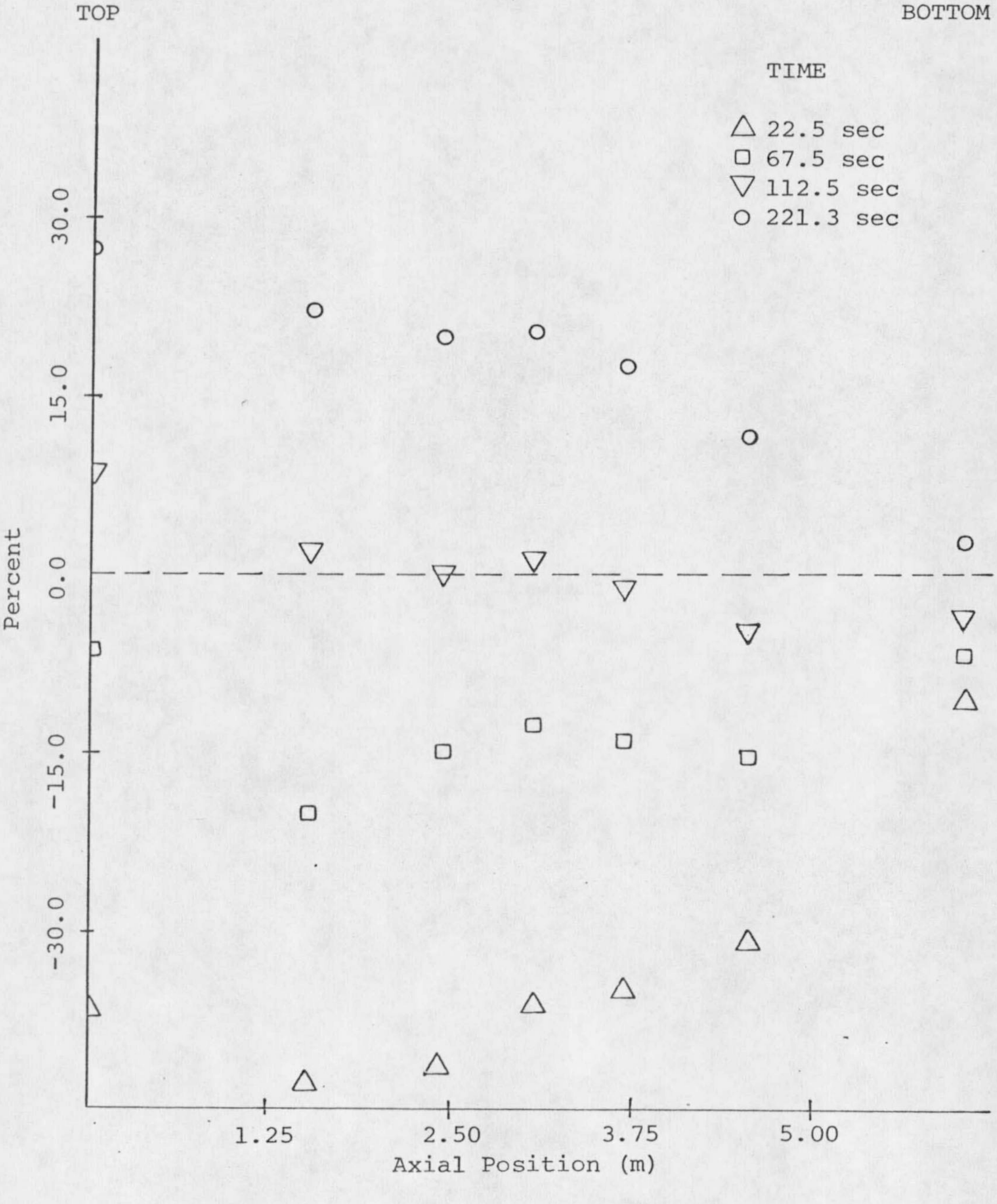

Figure 15. Percentage of Gas to Core Heat Transferred from the Core to the Containment Tube During a Steady State Blowdown Cycle.

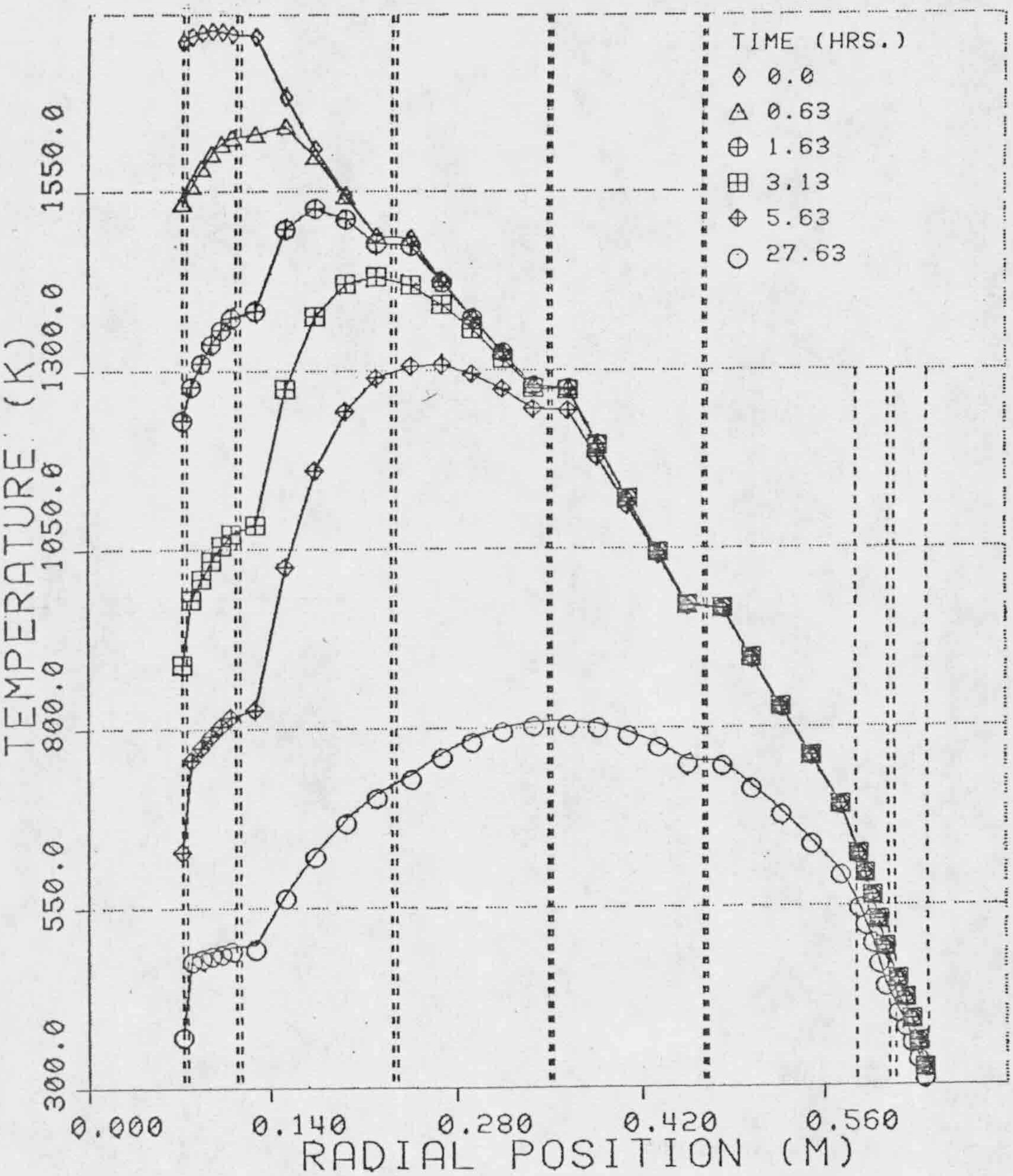

Figure 16. Radial Temperature Profile During Rapid Cooldown Axial Position 2.7 cm from Bed Top.

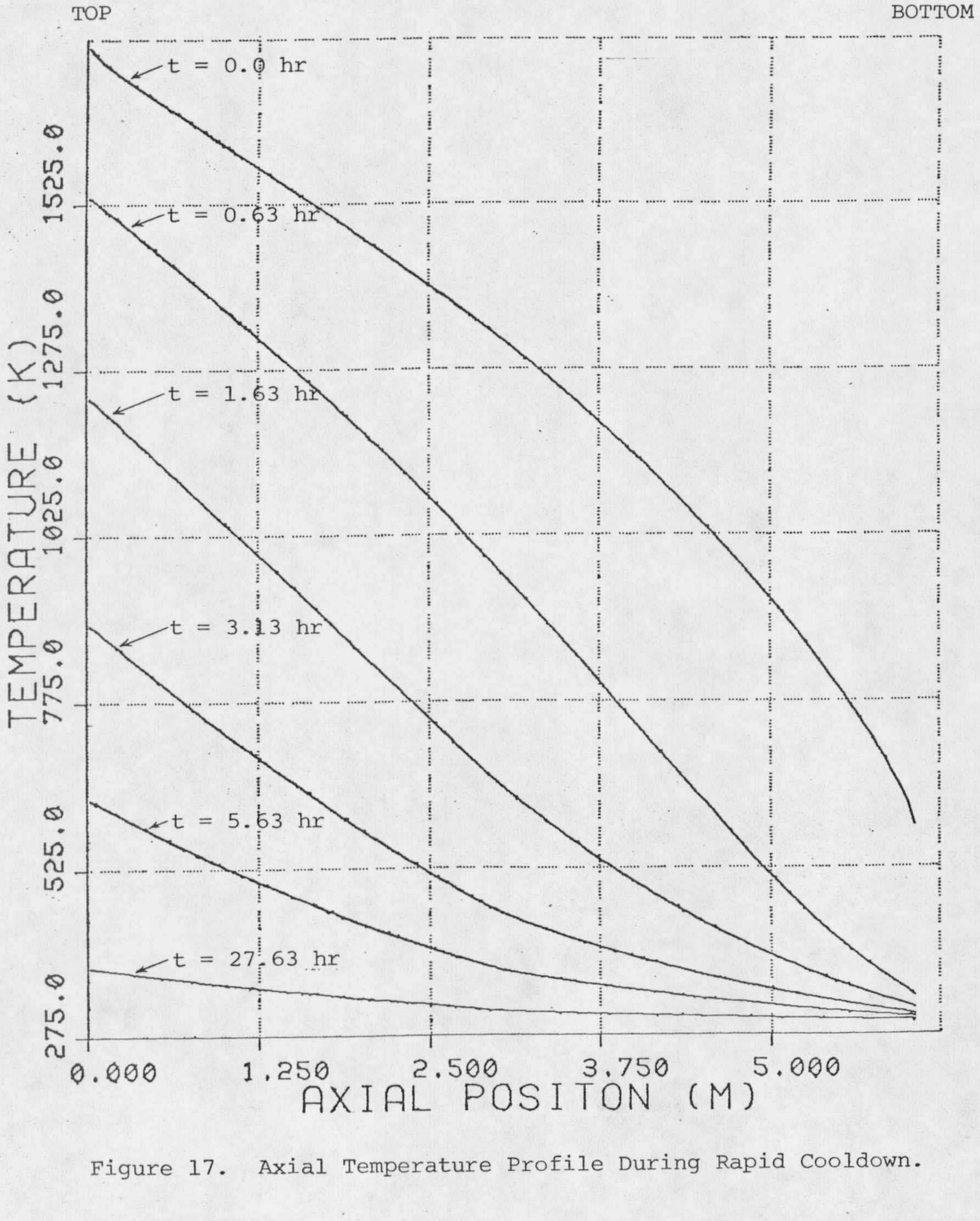

Figure 17. Axial Temperature Profile During Rapid Cooldown.

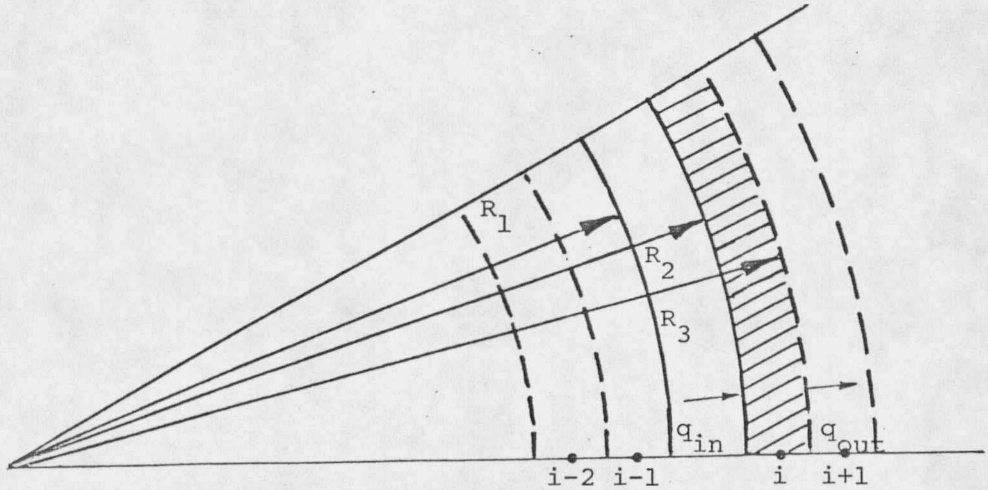

Figure 18a. An Inside Node.

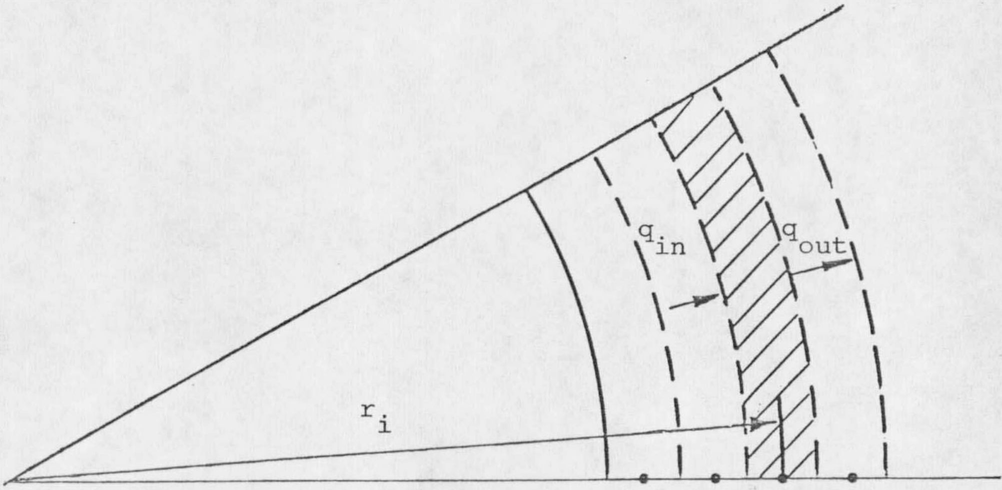

Figure 18b. An Interior Node.

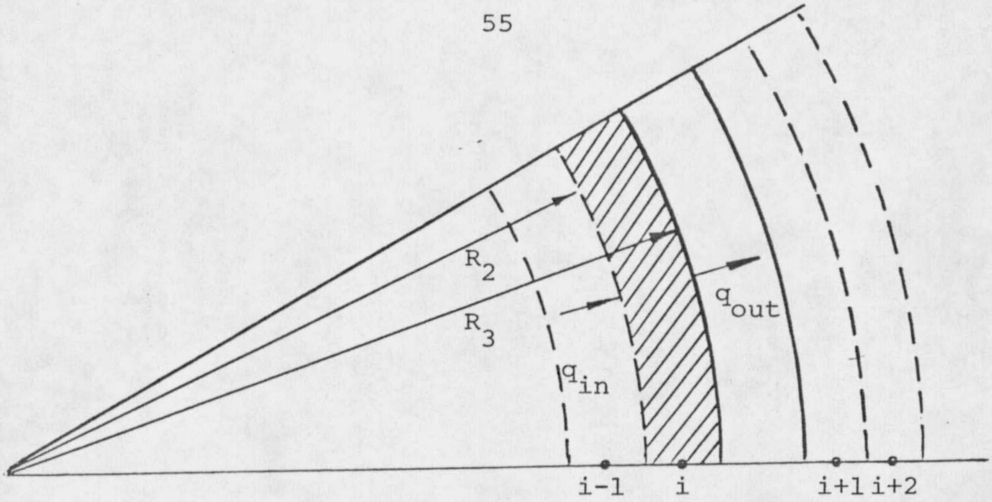

Figure 19a. An Outside Node.

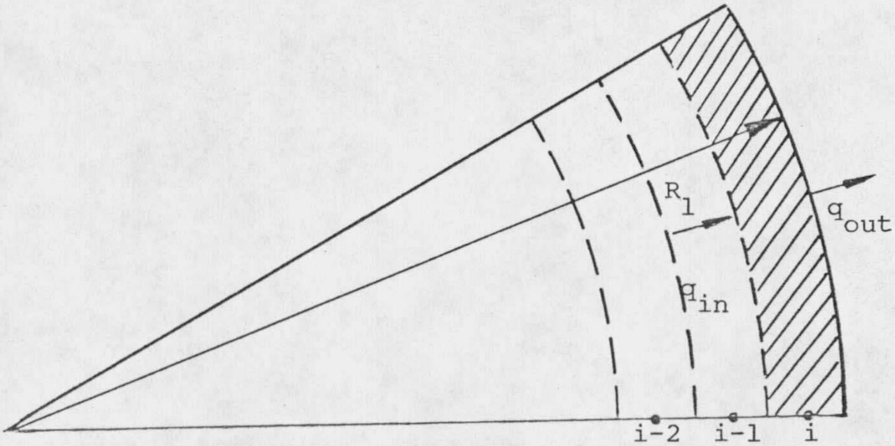

Figure 19b. The Outermost Node in the Radial Grid.

APPENDIXES

APPENDIX I

DERIVATION OF FINITE-DIFFERENCE EQUATIONS

Node at the Inside of an Insulation Layer

To develop the finite-difference equation for a node at the inside of an insulation layer, it is necessary to utilize the First Law of Thermodynamics as stated in Equation (13). From Equation (13) the rate of increase of internal energy of the system is equal to the net rate of heat transfer into the system when the work done by surface forces is equal to zero. The net rate of heat transfer into the system is the difference between the rate of heat transfer into the system and the rate of heat transfer leaving the system.

Referring to Figure 18a, the rate of heat transfer into increment i is equal to the rate of heat transfer through the vertical gap preceding increment i. From Equations (7) and (8) this rate of heat transfer can be written as

$$\dot{q}_{in} = \frac{\sigma A_1 (T_{i-1,j}^{4} - T_{i,j}^{4})}{\frac{1}{\varepsilon_{i-1}} + (\frac{A_1}{A_2})(\frac{1}{\varepsilon_i} - 1)} + (A_1 + A_2) h (T_{i-1,j} - T_{i,j})/2 \qquad (20)$$

where

$\dot{q}_{in}$ = heat into increment i (W)
(the dot [•] signifies a heat rate)

with an average area used in the natural convection term. The term R_1 as shown in Figure 18a, can be written as

$$R_1 = r_{i-1} + \frac{r_{i-1} - r_{i-2}}{2} = \frac{3}{2} r_{i-1} - \frac{1}{2} r_{i-2} \tag{21}$$

Likewise, R_2 can be written as

$$R_2 = r_i - \frac{r_{i+1} - r_i}{2} = \frac{3}{2} r_i - \frac{1}{2} r_{i+1} \tag{22}$$

Areas A_1 and A_2 can be written as

$$A_1 = 2\pi R_1 \Delta z = \pi \Delta z (3r_{i-1} - r_{i-2}) \tag{23}$$

$$A_2 = 2\pi R_2 \Delta z = \pi \Delta z (3r_i - r_{i+1}) \tag{24}$$

Substituting Equations (21) through (24) into Equation (20) gives

$$\dot{q}_{in} = \frac{\sigma\pi\Delta z(3r_{i-1}-r_{i-2})(T_{i-1,j}^{4}-T_{i,j}^{4})}{\frac{1}{\varepsilon_{i-1}} + \left(\frac{3r_{i-1}-r_{i-2}}{3r_{i-}-r_{i+1}}\right)\left(\frac{1}{\varepsilon_i}-1\right)}$$

$$+ h\pi\Delta z(3r_{i-1}-r_{i-2}+3r_i-r_{i+1})(T_{i-1,j}-T_{i,j})/2 \tag{25}$$

Referring to Equation (9), the rate of heat transfer out of increment i can be written as

$$\dot{q}_{out} = 2\pi\Delta z k_c(i)(T_{i,j}-T_{i+1,j})/\ell n(R_3/R_2) \tag{26}$$

where

$\dot{q}_{out}$ = rate of heat out of increment i (W)

and

$$R_3 = r_i + (r_{i+1}-r_i)/2 = 1/2\ r_i + 1/2\ r_{i+1} \qquad (27)$$

Equation (26) can be rewritten as

$$\dot{q}_{out} = \frac{2\pi\Delta z k_c(i)(T_{i,j}-T_{i+1,j})}{\ell n\left(\frac{r_i+r_{i+1}}{3r_i-r_{i+1}}\right)} \qquad (28)$$

The rate of heat storage in increment i can be written in differential form as

$$\dot{q}_s = \rho C_p V \frac{dT}{dt} \qquad (29)$$

In finite difference form Equation (29) becomes

$$\dot{q}_s = \rho(i)C_p(i)\pi\Delta z(R_3{}^2-R_2{}^2)(T_{i,j+1}-T_{i,j})/\Delta t \qquad (30)$$

where

$\dot{q}_s$ = rate of heat storage in increment i (W)

and

$$R_3{}^2 - R_2{}^2 = (r_i r_{i+1} - r_i{}^2)2 \qquad (31)$$

Equation (30) can then be rewritten as

$$\dot{q}_s = \rho(i)C_p(i)2\pi\Delta z r_i(r_{i+1}-r_i)(T_{i,j+1}-T_{i,j})/\Delta t \qquad (32)$$

Applying Equation (13), the energy equation, to increment i gives

$$\dot{q}_{in} = \dot{q}_{out} + \dot{q}_s \tag{33}$$

or using Equations (25), (28), and (32) in Equation (33)

$$\begin{aligned}
&\frac{\sigma\pi\Delta z(3r_{i-1}-r_{i-2})(T_{i-1,j}^{4}-T_{i,j}^{4})}{\frac{1}{\varepsilon_{i-1}} + \left(\frac{3r_{i-1}-r_{i-2}}{3r_i-r_{i+1}}\right)\left(\frac{1}{\varepsilon_i}-1\right)} + h\pi\Delta z(3r_{i-1}-r_{i-2}+3r_i-r_{i+1}) \\
&\quad \times (T_{i-1,j}-T_{i,j})/2 = \frac{2\pi\Delta z k_c(i)(T_{i,j}-T_{i+1,j})}{\ell n\left(\frac{r_i+r_{i+1}}{3r_i-r_{i+1}}\right)} + \rho(i)C_p(i)2\pi\Delta z \\
&\quad \times r_i(r_{i+1}-r_i)(T_{i,j+1}-T_{i,j})/\Delta t
\end{aligned} \tag{34}$$

Letting

$$\alpha_{12}(i) = \frac{\sigma(3r_{i-1}-r_{i-2})}{2\left[\frac{1}{\varepsilon_{i-1}} + \left(\frac{3r_{i-1}-r_{i-2}}{3r_i-r_{i+1}}\right)\left(\frac{1}{\varepsilon_i}-1\right)\right]} \tag{35}$$

$$\alpha_{13}(i) = h(3r_{i-1}-r_{i-2}+3r_i-r_{i+1})/4 \tag{36}$$

$$\alpha_{14}(i) = k_c(i)/\ell n[(r_i+r_{i+1})/(3r_i-r_{i+1})] \tag{37}$$

$$\alpha_{15}(i) = \rho(i)C_p(i)r_i(r_{i+1}-r_i)/\Delta t\ , \tag{38}$$

dividing both sides of Equation (34) by $2\pi\Delta z$, and using Equations (35) through (38), Equation (34) becomes

$$\alpha_{12}(i)[T_{i-1,j}^4-T_{i,j}^4]+\alpha_{13}(i)[T_{i-1,j}-T_{i,j}]$$

$$=\alpha_{14}(i)[T_{i,j}-T_{i+1,j}]+\alpha_{15}(i)[T_{i,j+1}-T_{i,j}] \qquad (39)$$

Rearranging Equation (39) to solve for $T_{i,j+1}$ gives

$$T_{i,j+1}=T_{i,j}+1/\alpha_{15}(i)\{\alpha_{12}(i)[T_{i-1,j}^4-T_{i,j}^4]$$

$$+\alpha_{13}(i)[T_{i-1,j}-T_{i,j}]-\alpha_{14}(i)[T_{i,j}-T_{i+1,j}]\} \qquad (40)$$

Equation (40) is used for all inside nodes except for the second node of the radial grid. Since node 1 is the outer boundary of the core, the terms defined in Equations (35) and (36) must be changed to become

$$\alpha_{12}(2)=\frac{\sigma r_1}{\frac{1}{\varepsilon_1}+\left(\frac{r_1}{1.5r_2-0.5r_3}\right)\left(\frac{1}{\varepsilon_2}-1\right)} \qquad (41)$$

and

$$\alpha_{13}(2)=h(r_1+1.5r_2-0.5r_3)/2 \qquad (42)$$

An Interior Node

An interior node is any node that is in the interior of any layer of insulation. To develop the finite-difference equation for an interior node, it is necessary to utilize the energy equation, Equation (13). Referring to Figure 18b, the rate of heat transfer into increment i is equal to the rate of heat transfer leaving increment i-1.

From Equation (28), the rate of heat transfer into increment i can be written as

$$\dot{q}_{in} = \frac{2\pi\Delta z k_c(i-1)(T_{i-1,j}-T_{i,j})}{\ln\left(\frac{r_{i-1}+r_i}{3r_{i-1}-r_i}\right)} \tag{43}$$

Equation (28) also describes the rate of heat transfer out of increment i, with a change in subscripts, and Equation (32) defines the rate of heat storage. Performing a heat rate balance, Equation (33) becomes

$$\frac{2\pi\Delta z k_c(i-1)(T_{i-1,j}-T_{i,j})}{\ln\left(\frac{r_{i-1}+r_i}{3r_{i-1}-r_i}\right)} = \frac{2\pi\Delta z k_c(i)(T_{i,j}-T_{i+1,j})}{\ln\left(\frac{r_i+r_{i+1}}{3r_i-r_{i+1}}\right)}$$

$$+ \rho(i)C_p(i)2\pi\Delta z r_i(r_{i+1}-r_i)(T_{i,j+1}-T_{i,j})/\Delta t \tag{44}$$

Dividing both sides of Equation (44) by 2πΔz and using the simplifications defined in Equations (37) and (38), Equation (44) becomes

$$\alpha_{14}(i-1)[T_{i-1,j}-T_{i,j}] = \alpha_{14}(i)[T_{i,j}-T_{i+1,j}] + \alpha_{15}(i)[T_{i,j+1}-T_{i,j}] \tag{45}$$

Rearranging and solving for $T_{i,j+1}$ gives

$$T_{i,j+1} = T_{i,j} + 1/\alpha_{15}(i)\{\alpha_{14}(i-1)[T_{i-1,j}-T_{i,j}]$$

$$- \alpha_{14}(i)[T_{i,j}-T_{i+1,j}]\} \tag{46}$$

Node at the Outside of an Insulation Layer

In order to derive a finite-difference equation for an outside node, it is necessary to perform a heat rate balance as defined by Equation (33) on the element defined by the particular outside node. Referring to Figure 19a, the rate of heat transfer into increment i can be defined by Equation (43). The rate of heat transfer out of increment i is due to natural convection and radiation in the vertical gap and is given by Equation (25), with a change in subscript, as

$$\dot{q}_{out} = \frac{\sigma\pi\Delta z(3r_i - r_{i-1})(T_{i,j}^4 - T_{i+1,j}^4)}{\frac{1}{\varepsilon_i} + \left(\frac{3r_i - r_{i-1}}{3r_{i+1} - r_{i+2}}\right)\left(\frac{1}{\varepsilon_{i+1}} - 1\right)}$$

$$+ h\pi\Delta z(3r_i - r_{i-1} + 3r_{i+1} - r_{i+2})(T_{i,j} - T_{i+1,j})/2 \qquad (47)$$

The rate of heat storage in increment i is defined by Equation (30). However, for an outside node, the term $R_3^2 - R_2^2$ becomes $2(r_i^2 - r_i r_{i-1})$ and Equation (30) can be written as

$$\dot{q}_s = \rho(i)C_p(i)2\pi\Delta z r_i(r_i - r_{i-1})(T_{i,j+1} - T_{i,j})/\Delta t \qquad (48)$$

Substituting Equations (43), (47), and (48) into Equation (33) gives

$$\frac{2\pi\Delta z k_c(i-1)(T_{i-1,j}-T_{i,j})}{\ell n(\frac{r_{i-1}+r_i}{3r_{i-1}-r_i})} = \frac{\sigma\pi\Delta z(3r_i-r_{i-1})(T_{i,j}^4-T_{i+1,j}^4)}{\frac{1}{\varepsilon_i}+(\frac{3r_i-r_{i-1}}{3r_{i+1}-r_{i+2}})(\frac{1}{\varepsilon_{i+1}}-1)}$$

$$+ h\pi\Delta z(3r_i-r_{i-1}+3r_{i+1}-r_{i+2})(T_{i,j}-T_{i+1,j})/2$$

$$+ \rho(i)C_p(i)2\pi\Delta z r_i(r_i-r_{i-1})(T_{i,j+1}-T_{i,j})/\Delta t \qquad (49)$$

By letting

$$\alpha_{18}(i) = \rho(i)C_p(i)r_i(r_i-r_{i-1})/\Delta t, \qquad (50)$$

dividing both sides of Equation (49) by $2\pi\Delta z$, and utilizing the simplifications given in Equations (35), (36), (37), and (50), Equation (49) becomes

$$\alpha_{14}(i-1)[T_{i-1,j}-T_{i,j}] = \alpha_{12}(i+1)[T_{i,j}^4-T_{i+1,j}^4]$$

$$+ \alpha_{13}(i+1)[T_{i,j}-T_{i+1,j}] + \alpha_{18}(i)[T_{i,j+1}-T_{i,j}] \qquad (51)$$

Rearranging Equation (51) to solve for $T_{i,j+1}$ gives

$$T_{i,j+1} = T_{i,j} + 1/\alpha_{18}(i)\{\alpha_{14}(i-1)[T_{i-1,j}-T_{i,j}]$$

$$- \alpha_{12}(i+1)[T_{i,j}^4-T_{i+1,j}^4]$$

$$- \alpha_{13}(i+1)[T_{i,j}-T_{i+1,j}]\} \qquad (52)$$

Equations (52) and (40) are used for nodes bordering a vertical gap except in the case when the temperature drop across a gap was considered negligible. This condition occurs when two adjacent insulating layers are in contact and any contact resistance is neglected. When two adjacent layers are in contact, a finite-difference equation similar to Equation (46) is used. The equation used for an inside node is

$$T_{i,j+1} = T_{i,j} + 1/\alpha_{15}(i)\{\alpha_{16}(i-1)[T_{i-1,j}-T_{i,j}] - \alpha_{14}(i)[T_{i,j}-T_{i+1,j}]\} \qquad (53)$$

where

$$\alpha_{16}(i-1) = k_c(i-1)/\ln[(3r_{i-1}-r_{i-2})/(r_{i-1}+r_{i-2})] \qquad (54)$$

For an outside node, the equation used when adjacent layers are in contact is

$$T_{i,j+1} = T_{i,j} + 1/\alpha_{18}(i)\{\alpha_{14}(i-1)[T_{i-1,j}-T_{i,j}] - \alpha_{16}(i)[T_{i,j}-T_{i+1,j}]\} \qquad (55)$$

The Outermost Node of the Radial Grid

To derive the finite-difference equation for the outermost node of the radial grid, it is necessary to again utilize a heat rate balance. Referring to Figure 19b, the rate of heat transfer into increment i is equal to that leaving increment i-1, as given by Equation (43). The heat storage rate in increment i is given by Equation (48). The heat rate out of increment i is by natural convection, given by Equations (7), (11), and (12), and by radiation, given by Equation (10). From Equations (7) and (10), the heat rate out of increment i can be written as

$$\dot{q}_{out} = \sigma\varepsilon_i 2\pi\Delta z R_1 (T_{i,j}{}^4 - T_\infty{}^4) + 2\pi\Delta z R_1 h (T_{i,j} - T_\infty) \tag{56}$$

The radial distance R_1 can be written as

$$R_1 = r_i + (r_i - r_{i-1})/2 = 3/2r_i - 1/2r_{i-1} \tag{57}$$

so that Equation (56) becomes

$$\dot{q}_{out} = \sigma\varepsilon_i \pi\Delta z (3r_i - r_{i-1})(T_{i,j}{}^4 - T_\infty{}^4) + h\pi\Delta z (3r_i - r_{i-1})(T_{i,j} - T_\infty) \tag{58}$$

Performing a heat balance on increment i using Equations (43), (48), and (58) gives

$$\frac{2\pi\Delta z k_c(i-1)(T_{i-1,j}-T_{i,j})}{\ell n\left(\frac{r_{i-1}+r_i}{3r_{i-1}-r_i}\right)} = \rho(i)C_p(i)2\pi\Delta z r_i(r_i-r_{i-1})$$

$$x\ (T_{i,j+1}-T_{i,j})/\Delta t + \sigma\varepsilon_i\pi\Delta z(3r_i-r_{i-1})(T_{i,j}{}^4-T_\infty{}^4)$$

$$+ h\pi\Delta z(3r_i-r_{i-1})(T_{i,j}-T_\infty) \qquad (59)$$

Letting

$$\alpha_{19}(i) = \sigma\varepsilon_i(3r_i-r_{i-1})/2 \qquad (60)$$

$$\alpha_{17}(i) = h(3r_i-r_{i-1})/2\ , \qquad (61)$$

dividing both sides of Equation (59) by $2\pi\Delta z$, and utilizing the simplifications defined by Equations (37), (50), (60), and (61), gives

$$\alpha_{14}(i-1)[T_{i-1,j}-T_{i,j}] = \alpha_{18}(i)[T_{i,j+1}-T_{i,j}]$$

$$+ \alpha_{19}(i)[T_{i,j}{}^4-T_\infty{}^4] + \alpha_{17}(i)[T_{i,j}-T_\infty] \qquad (62)$$

Rearranging Equation (62) to solve for $T_{i,j+1}$, Equation (62) becomes

$$T_{i,j+1} = T_{i,j} + 1/\alpha_{18}(i)\{\alpha_{14}(i-1)[T_{i-1,j}-T_{i,j}]$$

$$- \alpha_{19}(i)[T_{i,j}{}^4-T_\infty{}^4] - \alpha_{17}(i)[T_{i,j}-T_\infty]\} \qquad (63)$$

APPENDIX II

STABILITY CRITERIA FOR FINITE DIFFERENCE EQUATIONS

Since there are six types of finite-difference equations (14-17, 53, 55) used in this numerical technique, six separate stability analyses had to be completed. It was determined during the course of this investigation that the finite-difference equation defining the temperature change at the inside node of the last layer of insulation required the minimum time step Δt. For this reason the stability analysis at this node in the radial grid is shown here. Although not detailed here, a similar procedure was used to determine stability requirements for the other finite-difference equations.

The last layer of insulation used was a 25.4 mm thick layer of fiberglass insulation covering the steel shell. Since the gap between the steel shell and the insulation was negligible, Equation (53) was used for the inside node of this layer. Rearranging Equation (53) gives

$$T_{i,j+1} = T_{i,j}\{1 - \frac{\alpha_{16}(i-1)}{\alpha_{15}(i)} - \frac{\alpha_{14}(i)}{\alpha_{15}(i)}\} + \frac{\alpha_{16}(i-1)}{\alpha_{15}(i)} T_{i-1,j} + \frac{\alpha_{14}(i)}{\alpha_{15}(i)} T_{i+1,j} \tag{64}$$

Since the coefficient of $T_{i,j}$ must be positive, it can be seen from Equation (64) that

$$\frac{\alpha_{16}(i-1)}{\alpha_{15}(i)} + \frac{\alpha_{14}(i)}{\alpha_{15}(i)} < 1 \qquad (65)$$

or that

$$\alpha_{16}(i-1) + \alpha_{14}(i) < \alpha_{15}(i) \qquad (66)$$

The inequality given by Equation (66) specifies the condition that must be met in order to assure stability for the finite-difference method. From Equation (66), a maximum time step size can be calculated for a particular node structure by substituting values for the various terms.

From Equation (54), $\alpha_{16}(i-1)$ can be written as

$$\alpha_{16}(i-1) = k_c(i-1)/\ell n[(3r_{i-1}-r_{i-2})/(r_{i-1}+r_{i-2})] \qquad (67)$$

or

$$\alpha_{16}(i-1) = k_c(i-1)/\ell n[(r_{i-1}+\Delta r_{i-1}/2)/(r_{i-1}-\Delta r_{i-1}/2)] \qquad (68)$$

where

$$\Delta r_{i-1} = r_{i-1} - r_{i-2}$$

To simplify Equation (68), rewrite it as

$$\ell n \left[\frac{r_{i-1}+\Delta r_{i-1}/2}{r_{i-1}-\Delta r_{i-1}/2}\right] = \ell n \left[\frac{1+\Delta r_{i-1}/2r_{i-1}}{1-\Delta r_{i-1}/2r_{i-1}}\right] \qquad (69)$$

and expand the right hand side of Equation (69) using a logarithmic series [22].

$$\ell n \left[\frac{1+\Delta r_{i-1}/2r_{i-1}}{1-\Delta r_{i-1}/2r_{i-1}}\right] = 2\left[\frac{\Delta r_{i-1}}{2r_{i-1}} + \frac{1}{3}\left(\frac{\Delta r_{i-1}}{2r_{i-1}}\right)^3 + \frac{1}{5}\left(\frac{\Delta r_{i-1}}{2r_{i-1}}\right)^5 + \cdots\right] \quad (70)$$

Approximating the natural logarithm by the first term of the series gives

$$\alpha_{16}(i-1) = k_c(i-1)r_{i-1}/\Delta r_{i-1} \quad (71)$$

Using a similar expansion, $\alpha_{14}(i)$ can be written as

$$\alpha_{14}(i) = k_c(i)r_i/\Delta r_i \quad (72)$$

where

$$\Delta r_i = r_{i+1} - r_i \quad (73)$$

The remaining term in Equation (66) is given by Equation (38) as

$$\alpha_{15}(i) = \rho(i)C_p(i)r_i\Delta r_i/\Delta t \quad (74)$$

Substituting Equations (71), (72), and (74) into Equation (66) gives

$$\frac{k_c(i-1)r_{i-1}}{\Delta r_{i-1}} + \frac{k_c(i)r_i}{\Delta r_i} < \frac{\rho(i)C_p(i)r_i\Delta r_i}{\Delta t} \quad (75)$$

Rearranging to solve for Δt, Equation (75) becomes

$$\Delta t < \frac{\rho(i) C_p(i) r_i \Delta r_i}{\frac{k_c(i-1) r_{i-1}}{\Delta r_{i-1}} + \frac{k_c(i) r_i}{\Delta r_i}} \tag{76}$$

From Equation (76) an approximate maximum allowable time step can be determined for a particular radial length increment Δr. As an example, for five nodes per layer, Δr equals 5.08 mm, r_{i-1} equals 607 mm, and r_i equals 617 mm. Using the appropriate insulation properties, the maximum allowable time step is found to be approximately 4.8 seconds. Since some approximations were used in determining this value, a time step of 3 seconds was finally used to assure stability in this case.

REFERENCES

REFERENCES

1. Corman et al., "Energy Conversion Alternatives Study - General Electric Phase 1 Final Report," Lewis Research Center NASA, ERDA, NSF, NASA-CR 134948, 1976.

2. Nusselt, W., "Die Theorie des Winderhitzer," _Zeitschrift des Vereines deutcher Ingenieure_, Vol. 71, 1927, pp. 85-91.

3. Heiligenstaedt, W., "Die Berechnung von Warmespeichern," _Arch. Eisenhutte_., Vol. 4, 1928, pp. 217-222.

4. Rummel, K., "The Calculation of the Thermal Characteristics of Regenerators," _J. Inst. Fuel_, Feb. 1931, pp. 160-173.

5. Hausen, H., "Improved Calculations of the Thermal Characteristics of Regenerators," _Z. Ver. Deutsch. Ing_., Vol. 2, 1942, pp. 31-43.

6. Edwards, J.V., Evans, R. and Probert, S.D., "Computation of Transient Temperatures in Regenerators," _Int. J. Heat Mass Transfer_, Vol. 14, 1971, pp. 1175-1201.

7. Manrique, J.A. and Cardenas, R.S., "Digital Simulation of a Regenerator," _Int. Heat Transfer Conf_., 5th Proc., Vol. 5, 1974, pp. 190-194.

8. El-Rifai, M.A. and Taymour, N.E., "Temperature Transients in Fixed Bed Regenerators," _Chem. Eng. Sci_., Vol. 29, 1974, pp. 1687-1694.

9. Zakkay, V. and Speyer, D.M., "A High Reynolds Number Facility for Operation at 10000 psi and 3500 R," Aerospace Research Laboratories, May 1971.

10. Cook, G.S., "Evaluation of a Fossil Fuel Fired Ceramic Regenerative Heat Exchanger," OCR R&D Report 92 - Interim Report No. 1, Office of Coal Research, Department of the Interior, 1974.

11. Reihman, T.C., Townes, H.W. and Mozer, C.J., "Thermal Analysis Techniques for Regenerative Heat Exchanger Simulation," ASME Paper 76-WA/HT-7, 1976.

12. Jakob, M., _Heat Transfer_, Vol. 1, John Wiley and Sons, Inc., N.Y., 1949.

13. Holman, J.P., Heat Transfer, 3rd Ed., McGraw-Hill Book Co., N.Y., 1972.

14. Siegal, R. and Howell, J.R., Thermal Radiation Heat Transfer, McGraw-Hill Book Co., N.Y., 1972.

15. Kreith, F., Principles of Heat Transfer, 3rd Ed., McGraw-Hill Book Co., N.Y., 1973.

16. McAdams, W.H., Heat Transmission, 3rd Ed., McGraw-Hill Book Co., N.Y., 1954.

17. Rohsenow, W.M. and Hartnett, J.P. (eds.), Handbook of Heat Transfer, McGraw-Hill Book Co., N.Y., 1973.

18. Bolz, R.E. and Tuve, G.L., (eds.), Handbook of Tables for Applied Engineering Science, Chemical Rubber Co., Cleveland, 1970.

19. Technical Data Sheets, Harbison-Walker Refractories Co., Pittsburgh, Pa., 1976.

20. Technical Data Sheets, Johns-Manville Insulation Center, Denver, Colorado, 1976.

21. Steam/Its Generation and Use, The Babcock and Wilson Co., N.Y., 1975.

22. Selby, S.M., (ed.), Standard Mathematical Tables, CRC Press, Inc., Cleveland, 1975.

[redacted]

Ameel, Timothy A
Thermal simulation of an experimental high temperature fixed bed cored brick regenerative air preheater

[redacted]